Applied Catalysis A, General 616 (2021) 118098

Contents lists available at ScienceDirect

Applied Catalysis A, General

journal homepage: www.elsevier.com/locate/apcata

Influence of the initial state of ZrO_2 on genesis, activity and stability of Ni/ZrO_2 catalysts for steam reforming of glycerol

Sh.O. Omarov [a], D.A. Sladkovskiy [b], K.D. Martinson [a], M. Peurla [c], A. Aho [d], D.Yu. Murzin [d,*], V. I. Popkov [a]

[a] Laboratory of Materials and Processes for Hydrogen Energy, Ioffe Institute, Politekhnicheskaya Street 26, St. Petersburg, 194021, Russian Federation
[b] Laboratory of Catalytic Technologies, St. Petersburg State Institute of Technology, Moskovsky Ave. 26, St. Petersburg, 190013, Russian Federation
[c] Faculty of Medicine, University of Turku, 20014, Åbo/Turku, Finland
[d] Johan Gadolin Process Chemistry Centre, Åbo Akademi University, Biskopsgatan 8, 20500, Åbo/Turku, Finland

ARTICLE INFO

Keywords:
Zirconia
Nickel
Steam reforming
Glycerol
Activity
Stability

ABSTRACT

The effect of the initial state of ZrO_2 on properties of Ni/ZrO_2 catalysts for hydrogen production in steam reforming of glycerol was investigated. The catalysts were synthesized by impregnating the supports obtained by varying the treatment temperature of $ZrO_2 \cdot nH_2O$ and introducing Y_2O_3 as a promoter. All materials were characterized by thermal analysis, X-ray diffraction, N_2 physisorption, scanning electron microscopy, H_2-TPR, NH_3-TPD and transmission electron microscopy. The mutual influence of NiO and ZrO_2 on the genesis of the phase composition, pore structure and reducibility was demonstrated. Different catalytic behavior is explained by influence of the initial form of the support on the size, morphology of Ni particles, and the support thermal stability. The initial activity of Ni/$ZrO_2$is proportional to the monoclinic phase content. The catalysts based on tetragonal ZrO_2 displayed the best stability. For the first time, the presence of the aldol condensation products in glycerol steam reforming was demonstrated.

1. Introduction

Up to 50 % of all commercially available hydrogen is produced by steam reforming of methane. Natural gas reserves are, however, depleting which requires a search for new sources of hydrogen. One such potential feedstock can be a by-product of biodiesel manufacturing. Production of the latter has both advantages and disadvantages compared to petrodiesel [2–5]. Formation and accumulation of crude glycerol is one of the disadvantages, diminishing the its commercial value and capacity utilization. To overcome these challenges development of new and cost-effective ways for glycerol valorization are required [2]. Steam reforming [4,5], dry reforming [5,6], and aqueous-phase reforming [7–9] are possible routes for glycerol processing. Various reactions giving both gaseous products (H_2, CO, CO_2, etc.) and liquid products occur in these processes [5,10,11]:

SRG: $C_3H_8O_3 + 3H_2O = 7H_2 + 3CO_2$ ($\Delta H_{873\ K}$ =165.6 kJ/mol)

Glycerol decomposition: $C_3H_8O_3 = 4H_2 + 3CO$ ($\Delta H_{873\ K}$ =324.4 kJ/mol)

WGS: $3CO + 3H_2O = 3H_2 + 3CO_2$ ($\Delta H_{873\ K}$ = -52.9 kJ/mol)

Over the last years, a large number of papers has been published addressing various catalysts suitable for SRG. Judging by the literature not only the active phase, but also the support selection is very important. Because nickel is most often used as an active component [1,3,4,8, 12–15], the support should provide a high dispersion of Ni^0 particles, which is important for the structure-sensitive SRG [16], affecting also the catalyst stability. Coking and sintering as the main causes of SR catalysts deactivation largely depend on the support properties [5]. Optimally SRG is performed at high temperatures (> 873 K) giving high hydrogen yields, and allowing coke gasification at these temperatures range, thus mitigating deactivation. However, high process temperature requires adequate thermal stability of the catalyst, which is one of most challenging aspects for catalytic steam reforming of glycerol. Such a challenge is solved by selection both the process conditions and the support.

Abbrebiations: APR, aqueous phase reforming; MSI, metal-support interaction; SRG/SRE/SRM, steam reforming of glycerol/ethanol/methane; SSA, specific surface area; WGFR, water-to-glycerol feed ratio; WGS, water gas-shift reaction; YSZ, yttria-stabilized zirconia.

* Corresponding author.
E-mail address: dmurzin@abo.fi (D.Yu. Murzin).

https://doi.org/10.1016/j.apcata.2021.118098
Received 16 November 2020; Received in revised form 25 February 2021; Accepted 9 March 2021
Available online 15 March 2021

Catalysts based on ZrO_2, CeO_2 and SiO_2 show the best results among the most common supports (γ-Al_2O_3 [4–11,17,16,18], MgO, ZrO_2 [11, 19–21], CeO_2 [19], TiO_2, SiO_2 [11,20]). Comparison of Al_2O_3, ZrO_2, and SiO_2 as supports for SRG catalysts [11] revealed that Ni/ZrO_2 has a good stability, exceeding substantially that of Ni/Al_2O_3 being somewhat inferior to Ni/SiO_2. High stability of Ni/ZrO_2 was ascribed [11] to elevated inertness of the support, and a lower degree of coke graphitization in comparison with Ni/Al_2O_3. Manfro et al. [21] showed that the smallest amount of coke was observed on Ni/ZrO_2 compared to Ni/Al_2O_3 and Ni/CeO_2. A positive effect of zirconium on the catalytic properties is associated with two states of the close-to-surface ions (Zr^{4+}/Zr^{3+}), presence of oxygen vacancies, and weaker acidity of the zirconia surface [3,11,19,21–23].

Ni/ZrO_2 catalysts have been widely studied in steam reforming of glycerol [11,20,21,24–28], ethanol [30–33], ethylene glycol [34] and methane [29,35–38]. The phase composition [28] and the textural promoter [24,25,27] are the main parameters of ZrO_2 studied in the literature. It was shown in [25] that a catalyst based on YSZ with a tetragonal structure (t-ZrO_2) has a better activity than a catalyst based on unstabilized ZrO_2. At the same time, the authors [28,39,40] showed that the catalyst based on monoclinic ZrO_2 (m-ZrO_2) displays better activity and stability than the catalyst based on t-ZrO_2 for SRG, WGS and Cannizzaro reaction of pyruvaldehyde to lactic acid, respectively.

In addition to the tetragonal and monoclinic forms, ZrO_2 also exists in the amorphous state (am-ZrO_2) preceding the crystalline forms of ZrO_2. Amorphous ZrO_2 is obtained by precipitation of $ZrO_2{\cdot}nH_2O$ from zirconyl salts solutions. A study [41] of Ni/ZrO_2 catalysts for methane decomposition showed that am-ZrO_2 supported catalyst exhibited better activity and stability than the catalysts based on t- and m-ZrO_2. The results [41] were explained by an increased dispersion of Ni^0 on am-ZrO_2, as well as by a lower amount of coke and a degree of its graphitization on Ni/amZrO_2.

Either commercial zirconia [25,28,33] or ZrO_2 obtained under conditions of prolonged treatment of the precipitation product [28,41] were used. While full characterization of the physicochemical properties of the initial products is typically not provided, it can be still concluded that the initial state of the ZrO_2 precursor and the preparation conditions have a strong influence on the properties of the final zirconia support [42,43]. At the same time, contradictory results were reported regarding the effect of zirconia phase composition [25,28], where am-ZrO_2 was not considered as the initial support form for the SRG catalyst. In [28] the results on the effect of the zirconia phase composition on the Ni^0 particle size were not provided, and both commercial and homemade ZrO_2 were used as supports with different phase compositions. Therefore, there is a lack of information on the influence of the initial phase composition of ZrO_2, which can be represented by all three main modifications of ZrO_2 obtained from one precipitation product, on the catalytic behavior.

This work aims at elucidation of the effect of the initial state and structural modifications of ZrO_2 on the genesis of physicochemical properties, activity, selectivity and stability of Ni/ZrO_2 catalysts for hydrogen production in SRG. For the first time, all modifications of ZrO_2 (amorphous, stabilized and unstabilized t-ZrO_2 and m-ZrO_2) are investigated as supports of Ni/ZrO_2 catalysts for the SRG process, and changes in the state of the active component and support are monitored at the main stages of synthesis and testing. Close attention is paid to the comparison of the YSZ and m-ZrO_2 in terms of physicochemical properties, activity and stability. The initial form of ZrO_2 was controlled by varying the treatment temperature corresponding to the main stages of the transformation of $ZrO_2{\cdot}nH_2O$, and by introducing Y_2O_3 as a promoter. During catalytic testing the residence time was carefully selected allowing a fair comparison of different catalysts in terms of activity and stability. The results of this work are compared with the literature aiding in insightful selection of the phase composition of zirconia in Ni/ZrO_2 catalysts, and paving a way for further improvements of catalysts based on ZrO_2.

2. Experimental

2.1. Reagents

$ZrOCl_2{\cdot}8H_2O$ (chem. purity, Lenreactiv, Russia); $NH_3{\cdot}H_2O$ 25 wt.% (analytical grade, Lenreactiv, Russia); $Ni(NO_3)_2{\cdot}6H_2O$ (chem. purity, Neva-Reactiv, Russia); $Y(NO_3)_3{\cdot}6H_2O$ (chem. purity, Reachim, Russia).

2.2. Support preparation

$ZrOCl_2$ was used as a source for zirconium and $ZrO_2{\cdot}nH_2O$ was used as a precursor for ZrO_2. Precipitation of hydrous zirconia was done by rapid infusion of an aqueous solution of ammonia (25 wt.%) to 10 wt.% $ZrOCl_2$ solution. The synthesis conditions of $ZrO_2{\cdot}nH_2O$ are described in detail in [44].

Various ZrO_2 modifications were used as supports including:

- initial $ZrO_2{\cdot}nH_2O$, when the support is referred amZr;
- t-ZrO_2 и m-ZrO_2 obtained by heat treatment of 5−7 g of $ZrO_2{\cdot}nH_2O$ with the final temperatures of 703 and 873 K, respectively, giving the materials denoted as Zr703 and Zr873. The thermal treatment was carried out in a muffle furnace with a stepwise exposure to several temperature: 443 K and 523 K with the holding time of 0.5 h in both cases and at either 703 or 873 K for 2 h;
- yttria-stabilized zirconia denoted as 9YSZ, for which synthesis 1.632 g of $Y(NO_3)_3{\cdot}6H_2O$ was added to 5 g of $ZrO_2{\cdot}nH_2O$ and 5 mL of H_2O for the synthesis of a support with 9 wt.% Y_2O_3. The resulting suspension was evaporated at 333−343 K and periodic stirring until complete drying (2 h). The powder was thermally treated in a muffle furnace in a stepwise mode using the following program: 443 K – 0.5 h; 523 K – 0.5 h; 623 K – 0.5 h; 723 K – 0.5 h; 923 K – 2 h.

2.3. Catalyst preparation

NiO/ZrO_2 with 10 wt.% of NiO in the final composition of the thermal-treated catalyst was synthesized by the impregnation method. A solution of $Ni(NO_3)_2$ was first prepared using a required amount of NiO and distilled water based on a twofold excess relative to the total pore volume determined from N_2 physisorption. The amount of the support was taken to produce 3.33 g of NiO/support material. The resulting suspension was evaporated for 2 h at 333−343 K under periodic stirring until complete dryness. The powder was thermally treated in a muffle furnace in a stepwise mode according to the program: 443 K – 0.5 h; 523 K – 0.5 h; 623 K – 0.5 h; 723 K – 0.5 h; 873 K – 2 h. The samples prior and after reduction are denoted respectively as NiO/X or Ni/X, where X is the support name. The data on the NiO content in the synthesized samples are given in Table 1.

2.4. Characterization methods

2.4.1. Simultaneous TG-DTA

Thermogravimetry and DTA analysis were done with DTG-60A (Shimadzu). A sample of ca. 20−30 mg was heated in air to 1073 K with a temperature ramp of 10 K/min. The error of weight measurements was 1% and 1 μV for DTA.

2.4.2. X-ray diffraction (XRD)

XRD analysis was done using diff ;ractometer XRD-6100 (Shimadzu) for 2θ values 20−70° at 0.02°/step and 3 s/step exposition, Divergence slit : Scatter slit : Receiving slit = 0.5° : 0.5° : 0.15 mm, using CuK_α as a

Table 1
NiO content according to EDX data.

Sample	NiO/amZr	NiO/Zr703	NiO/Zr873	NiO/9YSZ
NiO, wt.%	9.9	10.8	10.6	11.9

source and Ni-filter. The processing of XRD patterns included the following stages: correction of the base line, smoothing over 15–21 points, subtracting the $K\alpha_2$-component ($K\alpha_2/K\alpha_1 = 0.5$). For analysis of XRD patterns the PDF-2 2016 software was applied. The ratio of integral intensities was calculated based on reflexes of the tetragonal t-ZrO_2 – $I_t(101)$ and monoclinic m-ZrO_2 – $I_m(111)$, $I_m(\bar{1}11)$ phases [46]:

$$X_m = \frac{I_m(111) + I_m(\bar{1}11)}{I_m(\bar{1}11) + I_m(111) + I_t(101)} \quad (1)$$

After transformation the volume based fraction (V_m) of m-ZrO_2 was calculated according to

$$V_m = \frac{P \cdot X_m}{1 + (1 - P) \cdot X_m} \quad (2)$$

where

$$P = \frac{H_t(101)}{H_m\left(\bar{1}11\right) + H_m(111)} \quad (3)$$

and H is the reflex intensity.

The size of t-ZrO_2, NiO and Ni crystallites (d_{XRD}, nm) was calculated based on the Scherrer equation, reflecting an inverse dependence of the crystal size on the width of the peak at half maximum ($K = 0.9$, $\lambda(CuK_{\alpha 1}) = 0.15406$ nm).

2.4.3. N_2-physisorption

Nitrogen physisorption was carried out with Autosorb 6iSA (Quantachrome) at 77 K. The samples were degassed at 523 K under vacuum up to residual pressure 12 Pa for 1 h. The surface area (SSA, m^2/g) was calculated using the multi-point Brunauer-Emmett-Teller (BET) method, while the average pore sizes (d_p, nm) and pore size distribution were assessed applying the DFT method, and the total pore volume (V_p, cm^3/g) was calculated at $p/p_0 \approx 0.99$.

2.4.4. Scanning electron microscopy (SEM-EDX)

SEM micrographs were obtained in BSE mode using a VEGA 3 SBH microscope (Tescan, Czech Republic). Energy dispersive X-ray spectroscopy (EDX) was performed in the same microscope using Oxford instruments INCAx–act.

2.4.5. Transmission electron microscopy (TEM)

The Ni/ZrO_2 samples were analyzed by transmission electron microscopy using a JEM-1400 PLUS microscope (JOEL ltd., Japan) at an accelerating voltage of 120 kV. For analysis, a sample was suspended in ethanol. A suspension drop was mounted on a copper grid coated with a holey carbon film. The size distribution, nickel particle diameter, the morphology of metal and support particles were retrieved from TEM images. The number average diameter (d_n, nm) and the surface-weighted nickel particle diameter (d_s, nm) were calculated from the size distribution in the following way:

$$d_n = \frac{\sum (n_i \cdot d_i)}{\sum (n_i)}; \quad (4)$$

$$d_s = \frac{\sum \left(n_i \cdot d_i^3\right)}{\sum \left(n_i \cdot d_i^2\right)}. \quad (5)$$

The dispersion for Ni^0 particles was calculated in the following way:

$$D(Ni) = \frac{6 \cdot V_m}{A_m \cdot d_s \cdot 10}, \quad (6)$$

where V_M is the atomic volume (10.95 $Å^3$), and A_M is the area occupied by a surface nickel atom (6.51 $Å^2$).

2.4.6. Thermal-programmed reduction (H_2-TPR) and desorption (NH_3-TPD)

H_2-TPR and NH_3-TPD was performed on Chemosorb (SOLO, Russia) with a thermal conductivity detector. For H_2-TPR the sample (ca. 98−102 mg) was pretreated in Ar (99.998 vol.% purity) at 573 K for 30 min, then heated to 1173 K at a ramp rate of 10 K/min under the 10 vol. % H_2/Ar mixture (18 mL/min Ar and 2 mL/min H_2). Isopropanol frozen in the liquid nitrogen (ca. 183−203 K) was used as a water trap. CuO was used as a reference for calibration of hydrogen consumption.

For NH_3-TPD a sample (ca. 111−114 mg) was pretreated in He (99.9999 vol.% purity) at 873 K for 30 min, then cooled to 386 K. The maximum temperature was limited by the sample reduction temperature (873 K) to avoid the effect of H_2O on the signal due to dehydration of the ZrO_2 surface [45]. The sample saturated with ammonia from a flow of 5 vol.% NH_3/He mixture (20 mL/min) at 386 K for 40 min was then purged with He flow (20 mL/min) for 30 min to remove the physisorbed ammonia. Ammonia desorption was carried out by heating the sample to 873 K at a rate of 10K/min in He flow (20 mL/min).

2.5. Catalytic experiments

Steam reforming of glycerol was carried out in a stainless steel reactor ($d_{inner} = 10$ mm, $L \approx 50$ cm) with a fixed catalyst bed at atmospheric pressure and 873 K. The set-up is shown in Fig. 1. The reactor furnace was designed to have three heating zones, which made it possible to expand the isothermal zone. Thermocouples to control the temperature in the reactor were installed on top of the quartz layer and below the catalyst layer, respectively. A pipe coil and a condenser were installed at the outlet of the reactor to condense the reaction products, followed by a separator for collecting the liquid products.

A sample powder was compressed on a press with a force of 2 tons into tablets (ø 13 mm), followed thereafter by their crushing to get the fraction of 0.14−0.5 mm, which was loaded into the reactor. The reactor was first exposed to a flow of N_2 (99.999 %, 30 mL/min), heated to 873 K and reduced at this temperature by neat H_2 (30 mL/min) for 0.5 h or 1 h for 0.13 g and 0.56 g of catalyst, respectively. After reduction, the reactor was purged in N_2 flow (100 mL/min) for 5 min.

Nitrogen and the water-glycerol solution were fed to the reactor. A mixture of 20 wt.% of glycerol and 80 wt.% of double distilled water was used as a feedstock giving WGFR of 20:1. The mixture was supplied by a LOIP LS-301 peristaltic pump through a silicone tube with a cross section of $d_{int}xd_{out} = 0.5 \times 2$ mm. Additional details of the catalytic experiments (catalyst volume, total liquid flow, N_2 flow rate) are given in the Figure captions in section 3.6 and Supporting Information.

The resulting gas mixture was accumulated in the gas holder for 5−7 min for sampling. The liquid products were drained from the separator immediately after the gas sample was taken. A probe of the gas phase products (50 mL) was taken into a GC glass syringe and analyzed on a Shimadzu GC-2010 Plus chromatograph with a thermal conductivity detector (capillary column RT-Msieve 5A, 30 m, $d_{inner} = 0.53$ mm and capillary column Rt-Q-BOND, 30 m, $d_{inner} = 0.53$ mm; temperature program: 303 K – 5 min; 303−333 K heating at rate 4 K/min; 333−373 K heating at rate 15°/min; 373–423 K heating at rate 30°/min; 423 K – 3 min; 423−453 K heating at rate 5°/min; 453 K – 23.9 min).

Catalytic behavior was evaluated in terms of glycerol conversion to gaseous products (X_{Ggas}, mol.%), hydrogen yield (Y_{H2}, mol H_2/mol glycerol), selectivity for H_2, CO_2, CO, CH_4, C_2H_4, C_2H_6, and C_3H_8 (S_i, mol.%) and turnover frequency of glycerol transformations (TOF_{Gly}, s^{-1}). The following equations were used to calculate the specified process indicators:

$$X_{Ggas} = \frac{Molar\ flow\ C\ from\ (CO_2 + CO + CH_4 + C_2H_4 + C_2H_6 + C_3H_8)}{Total\ C\ in\ the\ feedstock} \cdot 100\%, \quad (7)$$

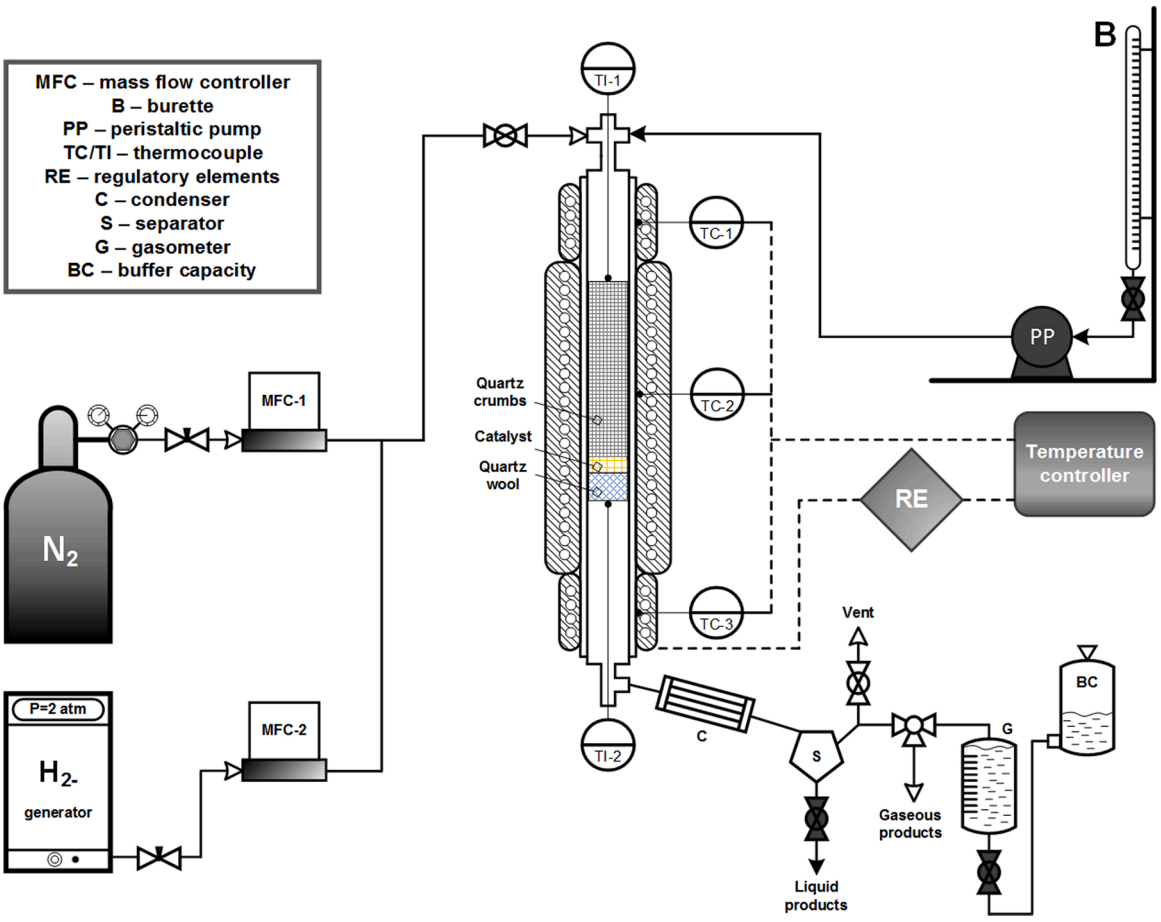

Fig. 1. Reactor set-up.

$$Y(H_2) = \frac{molar\ flow\ H_2}{moles\ glycerol\ in\ the\ feedstock}, \quad (8)$$

$$S(H_2) = \frac{Molar\ flow\ H_2}{Total\ molar\ flow\ C\ in\ gas\ products} \cdot \frac{3}{7} 100\%, \quad (9)$$

$$S_i = \frac{k \cdot Molar\ flow\ C\ from\ i}{Total\ molar\ flow\ C\ in\ gas\ products} \cdot 100\%, \quad (10)$$

where i – CO_2, CO, CH_4, C_2H_4, C_2H_6, C_3H_8;

k – number C atoms in the i;

total molar flow C = $n(CO_2) + n(CO) + n(CH_4) + 2 \cdot n(C_2H_4) + 2 \cdot n(C_2H_6) + 3 \cdot n(C_3H_8)$, mol/h.

$$TOF_{Gly} = \frac{N_{Gly}^{in} \cdot X_{Ggas} \cdot M(Ni)}{m_{cat} \cdot \omega(Ni) \cdot D(Ni) \cdot 3600}, \quad (11)$$

where N_{Gly} – initial molar flow of glycerol, mol/h; $M(Ni)$ – molar mass of Ni 58.71 g/mol; m_{cat} – catalysts mass, g; $w(Ni)$ – Ni loading in a catalyst, wt.%; $D(Ni)$ – nickel dispersion.

The composition of the reaction mixture was analyzed by high performance liquid chromatography (HPLC) on a Hewlett Packard 1100 series with a refractive index detector (RI). The column used for the separation of the compounds was an Animex HPX-87H applying 5 mM sulfuric acid as the eluent. The temperature of the column was 318 K and the flow of H_2SO_4 was 0.6 mL/ min. The response factors and retention times for several different compounds were determined prior to catalytic experiments and used for calculations of the concentrations.

The calculation of the liquid products distribution in the probe accumulated over the entire period of the stability test of the catalysts (TOS = 12 h) was carried out using the following formula, excluding unconverted glycerol:

$$S_i = \frac{k \cdot Molar\ amount\ C\ from\ i}{Total\ molar\ amount\ C\ in\ liquid\ products} \cdot 100\%, \quad (12)$$

where i – mannitol, glyceraldehyde, erythritol, pyruvaldehyde, 1,3-dihydrohyacetone, acetic acid, ethylene glycol, hydroxyacetone, 2,3-dutandiole, 1,4-butandiole, ethanol + allylic alcohol, 2-propanol.

The calculation of the Mears and Weisz-Prater criteria was carried out to assess the effect of external and internal diffusion respectively [47]. An example of calculations is provided in the Supporting Information.

3. Results and discussion

3.1. Phase composition and texture of the supports

The results for the initial support (Simultaneous thermal analysis, XRD, pore distribution) are presented in the Supporting Information and Table 2.

During the thermal treatment of the starting X-ray amorphous amZr ($ZrO_2 \cdot nH_2O$) three main stages can be identified (Fig. S1): dehydration with the formation of amorphous ZrO_2; crystallization of am-ZrO_2 in the temperature range 673−738 K; a polymorph transformation of t-ZrO_2 to m-ZrO_2. A mixture of crystalline phases t-ZrO_2 and m-ZrO_2 (Fig. S2, curve 2) with predominantly t-ZrO_2 (74 vol.%, Table 2) presence is formed at the end of crystallization (Zr703 support). The phase transition t-ZrO_2 → m-ZrO_2 proceeds with a further rise in the temperature to 873 K (Zr873 support) giving as a result mainly m-ZrO_2 (86 vol.%). It should be noted that small amounts of the residual amorphous component might remain in the Zr703 sample due to thermal treatment in the

Table 2
Phase composition and pore structure for the support and NiO/ZrO_2.

Sample	Phase composition			Texture		
	Phases	V_m, vol.%	d_{XRD} for NiO, nm	SSA, m^2/g	V_p, cm^3/g	d_p, nm
Supports						
amZr	a	–	–	252	0.192	3.0
Zr703	t + m	26	–	84	0.184	8.8
Zr873	m + t	85	–	44	0.183	16.7
9YSZ	t	0	–	64	0.180	11.2
NiO/ZrO_2						
NiO/amZr	t + NiO	0	10.6	57	0.194	24.2
NiO/Zr703	m + t + NiO	77	15.1	39	0.145	15.0
NiO/Zr873	m + t + NiO	92	18.7	31	0.139	17.7
NiO/9YSZ	t + NiO	0	18.2	43	0.148	13.8

crystallization region of am-ZrO_2 [48].

This behavior of ZrO_2 corresponds to generally accepted concepts of the genesis of $ZrO_2{\cdot}nH_2O$ obtained by precipitation from zirconyl salts [49]. An increased pH of precipitation favors formation of predominantly t-ZrO_2 after crystallization of a-ZrO_2 [50]. The tetragonal form is transformed into the monoclinic form of ZrO_2 with an increase in the processing temperature because some of t-ZrO_2 crystallites reach their critical size of 30 nm [51].

Addition of Y_2O_3 (support 9YSZ) from $Y(NO_3)_3$ leads to appearance of a new endo peak on the DTA curve, a strong peak of the weight loss on the DTG curve in the range of 573–703 K, and a shift of the crystallization peak of a-ZrO_2 by 24°. The phase composition of 9YSZ support is represented by tetragonal or cubic ZrO_2 after thermal treatment at 923 K (Fig. S2, curve 3). The presence of a weak reflection at 2θ of 43.14° indicates that the phase composition of 9YSZ is represented by a tetragonal ZrO_2. On the other hand, in the phase diagram of Y_2O_3-ZrO_2 [53–55], at Y_2O_3 content of 9 wt.% (or 5 mol.% Y_2O_3) the phase composition is represented by a mixture of m- and c-ZrO_2. However, the synthesis conditions for 9YSZ in the current work are close to [52] not corresponding at the same time to the equilibrium ones. Calculation of the unit cell parameters for 9YSZ sample in the tetragonal syngony approximation ($P4_2nm(c)$) gives the values a = b = 0.361(5) nm and c = 0.515(2) nm, which are in agreement with the results [52] for yttria content of 9 wt.%. Thus, 9YSZ is a well-crystallized thermostable support of the tetragonal modification.

A change in the porous structure occurs during the described phase transitions of zirconia (Table 2, Fig. S3). The initial $ZrO_2{\cdot}nH_2O$ has a micro-mesoporous structure, which corresponds to the pore size distribution mainly in the region of 1–4 nm. This is also evidenced by the presence of a region of strong nitrogen sorption at low p/p_0, characteristic of type I isotherms, and also of H4 hysteresis loop type [56]. Thermal treatment at 703 K leads to a decrease in SSA to 84 m^2/g. At the same time, there is also a strong change in the pore size distribution (Fig. S3) and the average pore size towards larger sizes (from 3.0 for Zr703 to 16.7 nm for Zr873, Table 2). Addition of Y_2O_3 promotes some improvement of the porous structure, which can be seen from an increase in SSA (by 20 m^2/g compared to Zr873) and a shift in the pore distribution downward (11.2 nm for 9YSZ compared to 16.7 nm for Zr873). This improvement of the porous structure is associated with stabilization of t-ZrO_2, which has a lower density and a particle size compared to m-ZrO_2.

Thus, thermal treatment of $ZrO_2{\cdot}nH_2O$ at temperatures of the main transformations of $ZrO_2{\cdot}nH_2O$ makes it possible to obtain supports of various phase composition, thermal stability, and porous structure. Addition of Y_2O_3 as a promoter helps to stabilize t-ZrO_2 and reduce sintering of the support structure.

3.2. Thermal transformations and phase composition for NiO/ZrO_2

The DT-curves of the synthesized non-heat-treated nickel-zirconia samples are shown in Fig. 2, while diffractograms of NiO/ZrO_2 after thermal treatment of the impregnated compositions are shown in Fig. 3.

The exopeak of am-ZrO_2 crystallization (NiO/amZr sample, Fig. 2, curve 1) is shifted towards higher temperatures when NiO is deposited from $Ni(NO_3)_2$ on the initial $ZrO_2{\cdot}nH_2O$ and crystallization proceeds in a broader temperature range (673–923 K) in comparison with the initial $ZrO_2{\cdot}nH_2O$ (Fig. S1). A set of several endopeaks with distorted shapes and positions relative to the decomposition peaks of $Ni(NO_3)_2{\cdot}6H_2O$ is observed when NiO was deposited on crystalline supports (Fig. 2, curves 2–4). It is clearly seen in the temperature range 293–523 K where physically and chemically adsorbed H_2O is removed. The peak at ca. 573 K apparently corresponds to the decomposition of the nitrate-containing intermediate compound with the formation of NiO, however, this peak is shifted by +50K compared to the initial $Ni(NO_3)_2$ [57]. The shift of the peaks can be due to several reasons: different interactions with the support surface functional groups, influence of the porous structure on the rate of decomposition products removal, etc. The NiO precursor decomposition process is significantly different from others supports when NiO was deposited on the amZr support. The presence of only two weak endopeaks in the range of 573–723 K indicates a stronger change in the decomposition of $Ni(NO_3)_2$.

The current data show that addition of Y_2O_3 or NiO had a different effect on the thermal transformations of the corresponding binary systems. Decomposition of $Y(NO_3)_3$ and $Ni(NO_3)_2$ deposited on amZr did not display the corresponding individual peaks of nitrate decomposition in the region of thermograms before the onset of am-ZrO_2 crystallization. At the same time, crystallization of am-ZrO_2 changes more noticeably with the introduction of NiO than Y_2O_3. Duchet et al. [58] also observed similar differences in the behavior of these systems without, however, a detailed discussion. The obtained data indicate occurrence of a reaction between $Ni(NO_3)_2/Y(NO_3)_3$ with $ZrO_2{\cdot}nH_2O$ during impregnation, which was reported in [52,58–60] for Y_2O_3/ZrO_2. For example, it was indicated [52] that $[(Zr_{4(1-x)}Y_{4x}(OH)_8(OH)_2)_{16}]^{(8-4x)+}$ ion is formed in a solution of zirconium and yttrium nitrates, subsequently determining formation of a solid solution and stabilization of t(c)-ZrO_2. This was shown by thermal analysis and XRD for Y_2O_3/ZrO_2 and MgO/ZrO_2 in [59,60]. A similar effect appeared in this work, namely a partial re-dissolution of $ZrO_2{\cdot}nH_2O$ in acidic solutions of $Y(NO_3)_3$ and $Ni(NO_3)_2$ occurs during impregnation, generating mixed compounds.

In addition, results of the thermal analysis determine a choice of a

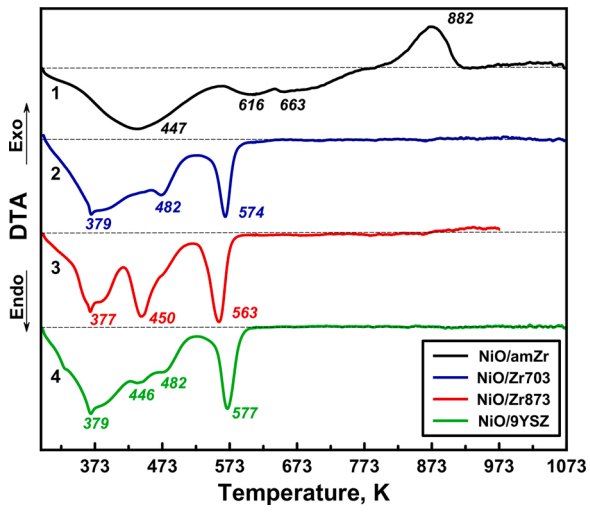

Fig. 2. DTA-curves for non-thermally treated composites: 1 – NiO/amZr; 2 – NiO/Zr703; 3 – NiO/Zr873; 4 – NiO/9YSZ (— – zero line).

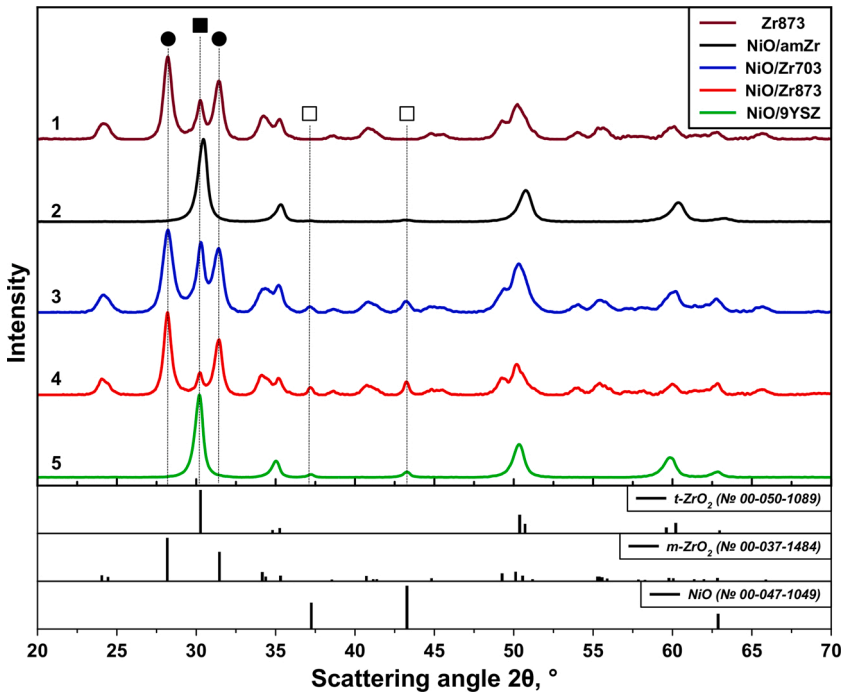

Fig. 3. XRD patterns of as-prepared samples: 1 – Zr873; 2 – NiO/amZr; 3 – NiO/Zr703; 4 – NiO/Zr873; 5 – NiO/9YSZ (● – m-ZrO_2; ■ – t-ZrO_2; □ – NiO).

stepwise thermal treatment procedure able to avoid sharp changes in the samples temperature during decomposition and crystallization.

XRD confirmed that NiO/ZrO_2 exhibits a mixture of different phases. Reflexes at 2θ values of 37.24° and 43.27° (Fig. 3) indicate presence of NiO in the cubic modification (Fm3m, PDF N⁰00-047-1049) in all samples. The size of the coherent scattering region d_{NiO} strongly depends on the support type (Table 2) increasing in the order NiO/amZr < NiO/Zr703 < NiO/Zr873 ≈ NiO/9YSZ. At the same time, NiO affects the phase formation of ZrO_2. The m-ZrO_2 phase is absent in NiO/amZr and NiO/9YSZ (Fig. 3, Table 2), which indicates strong stabilization of the t-ZrO_2 phase by nickel oxide. However, the t-ZrO_2 reflections in NiO/amZr are shifted relative to the corresponding t-ZrO_2 reflections in NiO/9YSZ and the reference diffractogram. Various works indicate that NiO stabilizes either c-ZrO_2 [61] or t-ZrO_2 [62,63]. However, the region of solid solutions is absent in the phase diagram of NiO-ZrO_2. A detailed analysis of diffractograms by the Rietveld refinement confirmed [62] stabilization of especially t-ZrO_2 by NiO with, however, lower unit cell parameters than for unmodified t-ZrO_2. Calculations of the t-ZrO_2 lattice parameters with the $P4_2/nmc$ structure type for NiO/amZr gave a = 3.595 Å and c = 5.081 Å in good agreement with [62]. The presence of free NiO reflections in this sample indicates a limited solubility of NiO in ZrO_2, which according to [62] is 5 mol.%. Nickel oxide remains on the surface of NiO/amZr rather than forming a solid solution with zirconia. It should be noted that the size of NiO particles in NiO/amZr is significantly smaller (d_{NiO} = 10.6 nm) than in other materials. A more detailed study of am-ZrO_2 crystallization in NiO/amZr by *ex-situ* XRD partially explains a decreased value of d_{XRD}. To this end NiO/amZr was thermally treated at different temperatures: 713, 773 and 823 K not showing any NiO reflections up to 823 K. These results are in line with the thermal analysis indicating strong interactions between $Ni(NO_3)_2$ and $ZrO_2{\cdot}nH_2O$.

NiO/Zr703 and NiO/Zr873 samples exhibit t-ZrO_2 and m-ZrO_2 in different ratios. A decrease of the transition from t-ZrO_2 to m-ZrO_2 is observed in NiO/Zr703, however, to a lesser extent than in NiO/amZr. Apparently, this is due to a slower growth of t-ZrO_2 crystallites to the critical size hindering a further transition to m-ZrO_2. It should be noted that an insignificant fraction of am-ZrO_2 may remain in Zr703 support [48] which interacts with $Ni(NO_3)_2$. This leads to partial stabilization of t-ZrO_2 during a further thermal treatment. At the same time, NiO reflections on the crystallized supports (Zr703, Zr873, 9YSZ) were detected already after thermal treatment at 703 K, i.e. after completion of Ni$(NO_3)_2$ decomposition. The phase composition of the 9YSZ support in NiO/9YSZ did not change after deposition of $Ni(NO_3)_2$ and subsequent thermal treatment. According to Table 2, there are no significant differences in the size of NiO particles depending on the phase composition of the thermostable support (m-ZrO_2 in Zr873 and t-ZrO_2 in 9YSZ).

Thus, the mutual influence NiO and ZrO_2 is determined by the initial form of zirconia. The pretreatment temperature of ZrO_2 and the introduction of NiO make it possible to regulate the phase composition of the synthesized samples, which can affect catalytic activity. The content of t-ZrO_2 increases in the order NiO/Zr873 < Ni/Zr703 < Ni/amZr for the samples obtained using non-promoted ZrO_2. The size of NiO particles is reciprocal to the fraction of m-ZrO_2, being almost independent of the phase composition for the thermostable supports (m-ZrO_2 in Zr873 and t-ZrO_2 in 9YSZ).

3.3. *NiO/ZrO_2 porous structure*

The porous structure of NiO/ZrO_2 is inextricably linked with the phase composition described above. The data for the porous structure of NiO/ZrO_2 are shown in Fig. 4 and Table 2.

The obtained N_2 sorption isotherms are close to the type IV according to the IUPAC classification [56] which is due to the presence of an inflection point in the region p/p_0 = 0.75–0.95. The hysteresis loops correspond to the H3 type, indicating presence of a sufficient number of large pores. The results of scanning electron microscopy (Fig. 5) are consistent with the N_2 sorption data, namely, that the particles of powdered Zr873 are mainly sintered aggregates of plate particles. A series of images shows that the most sintered samples (Zr873, NiO/Zr873) correspond to a more distinct manifestation of a lamellar morphology due to bulk sintering and appearance of wider micro-cracks (corresponding apparently to macropores). At the same time, there were no noticeable differences between the particles morphology of NiO-containing samples synthesized based on different supports.

The increased specific surface area of NiO/amZr and NiO/YSZ materials is mainly due to the phase composition formed by t-ZrO_2 which

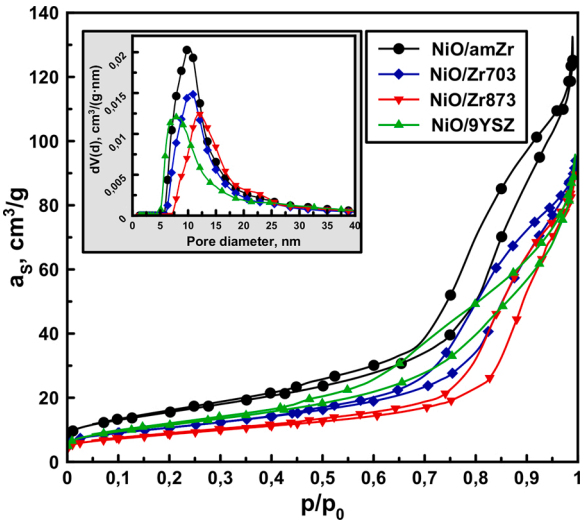

Fig. 4. N_2 adsorption-desorption isotherms and the pore size distribution curves.

has a lower density compared to m-ZrO_2. Appearance of large amounts of m-ZrO_2 (Table 2) leads to a significant decrease in SSA. The predominant pore diameter is in the range 5−20 nm as can be seen from Fig. 4. A shift of the distribution towards larger sizes is observed depending on the initial state of the support. A comparison of the pore volumes of the supports and NiO/ZrO_2 indicates that the pores are filled with nickel oxide in the case of NiO/Zr873 and NiO/9YSZ. For NiO/amZr an increased pore volume and SSA were observed compared to Zr873. This can be explained by absence of the transition from t-ZrO_2 to m-ZrO_2 after NiO deposition and subsequent heat treatment, indicating slower sintering of bulk ZrO_2. Introduction of Y_2O_3 (i.e. 9YSZ and NiO/9YSZ) has a similar effect. While somewhat similar results for NiO/ZrO_2 were reported in the literature [31,58,61,64], a positive effect of NiO on the porous structure of NiO/ZrO_2 when the latter is prepared from amorphous $ZrO_2{\cdot}nH_2O$, was not mentioned.

In summary synthesized NiO/ZrO_2 materials have a meso-macroporous structure. The specific surface area of NiO/ZrO_2 decreases with an increase in the pretreatment temperature of ZrO_2 in the order NiO/amZr – NiO/Zr703 – NiO/Zr873. Nickel oxide supported on $ZrO_2{\cdot}nH_2O$ similarly to Y_2O_3 prevents sintering of ZrO_2 and improves the textural characteristics of NiO/ZrO_2. The presence of relatively wide pores can be advantageous diminishing internal mass transfer limitations.

3.4. NiO/ZrO_2 reducibility and Ni^0 particle size

NiO/ZrO_2 reduction profiles are shown in Fig. 6 The main part of hydrogen is consumed in the temperature range from 623 to 890 K. The split between different regions is shown in Table 3.

In different temperature regions NiO is reduced with a varying degree of interactions with the support [25,29,61,65]. Bulk NiO weakly interacting with ZrO_2 is reduced at temperatures below 773−823 K (region α). Medium strength interactions of nickel oxide with ZrO_2 allow reduction in the temperature range between 773–923 K (region β). There is a tendency for an increase in the amount of absorbed hydrogen in the temperature range 623−893 K with an increase in the temperature of the preliminary treatment of zirconia (NiO/amZr < NiO/Zr703 < NiO/Zr873). This indicates an increase in the amount of NiO interacting weakly and moderately with ZrO_2. NiO/9YSZ has the largest amount of hydrogen consumed for its reduction in this interval. An increase in the fraction of NiO, weakly interacting with ZrO_2, correlates with an increase in d_{NiO} (Table 2). A poorly visible reduction peak at 893−1173 K (region γ) is observed in the TPR profile of NiO/amZr. Intensity of this peak significantly decreases with an increase in the ZrO_2 pretreatment temperature to 703 K (NiO/Zr703). A comparison with XRD data (Fig. 3) shows that NiO is reduced from a solid solution with zirconia in the γ temperature range.

Deconvolution of the main reduction peak by a set of Gaussian functions shows that two peaks characterize the α- and β-region similar to [25]. It was reported [66,67] that each of the peaks corresponds to a part of NiO interacting with a particular ZrO_2 phase. However, based on XRD data (Fig. 3) and TPR (Fig. 6) the result for NiO/ZrO_2 obtained under the conditions described above [67] cannot be confirmed. It is possible that such behavior is pronounced only at high thermal treatment temperatures.

The XRD results of the samples reduced at 873 K in the catalytic reactor are shown in Fig. 7 and Table 3. Ni/ZrO_2 differs substantially from NiO/ZrO_2 in several respects.

First, there is an increase in the particles of the deposited component. After reduction, the sample on the amZr support exhibits the largest increase in the coherent scattering region from 10.6 nm NiO to 21.1 nm Ni^0. This observation is due to the surface mobility, intergrowth and/or coalescence of Ni^0 particles formed during the reduction of fine NiO particles and Ni^{2+} from a solid solution in ZrO_2. However, some unreduced Ni^{2+} dissolved in ZrO_2 remains in Ni/amZr, (Figs. 6 and 7). An increase in Ni^0 particle size as compared with NiO after NiO/ZrO_2 reduction is noted in some studies [11,65–67]. However, the difference between d_{Ni} and d_{NiO} decreases with an increase in the pretreatment temperature of the support and for the samples, being almost negligible on Zr873 and 9YSZ supports within the measurement error.

Second, changes of the phase composition of ZrO_2 were clearly

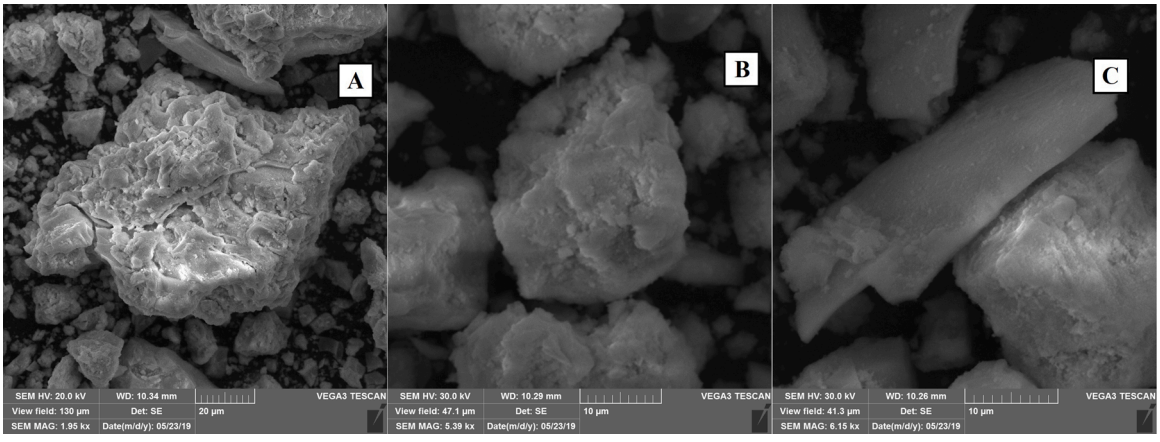

Fig. 5. SEM images of Zr873 (A), NiO/Zr873 (B), NiO/9YSZ (C).

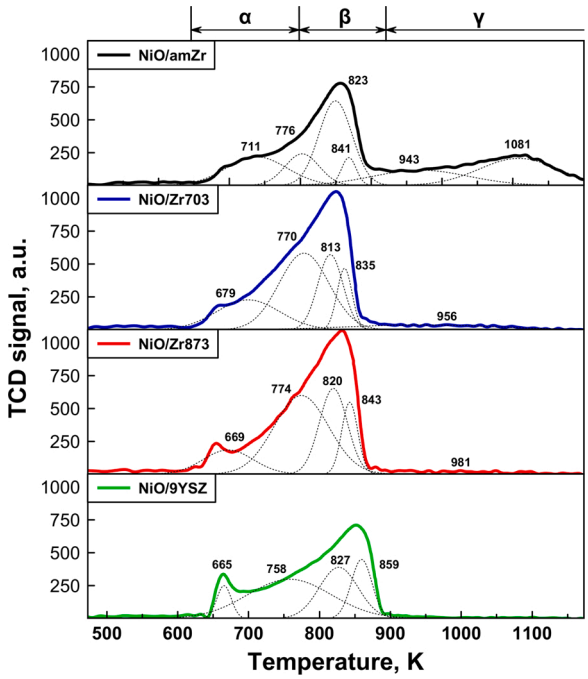

Fig. 6. H_2-TPR profiles for NiO/ZrO_2.

visible especially for amZr and Zr703 support. NiO/amZr contains m-ZrO_2, because of a partial reduction of Ni^{2+} from the solid solution with ZrO_2 and a loss of stability of large t-ZrO_2 crystallites. A schematic representation of this process (excluding the particle morphology) is presented in Fig. 8. A change in the position of the t-ZrO_2 reflections also confirms this assumption, which can be seen from the c lattice parameter of t-ZrO_2 equal respectively to 5.081 Å for unreduced NiO/amZr and 5.149 Å for Ni/ZrO_2. NiO/Zr703 also undergoes a phase transition from t-ZrO_2 to m-ZrO_2 after reduction with an increase in V_m to 89 vol.%. No changes in the phase composition of the support were observed after reduction for Ni/9YSZ and Ni/Zr873 samples.

The catalysts reduced at 873 K in the catalytic reactor were additionally studied by TEM to determine the morphology and the particle size of Ni^0 (Figs. 9 and S4). Zirconia supports are represented by elongated rounded particles sintered together. Particles of 9YSZ in Ni/9YSZ have a polycrystalline structure, while amZr in Ni/amZr is characterized by the least sintered structures compared to Zr873 in Ni/Zr873. It was noted [68,69] that Ni^0 particles are indistinguishable from ZrO_2 particles due to a weak contrast. Particles darker than ZrO_2, apparently corresponding to Ni^0, are visible in Fig. 9. The hexagonal raft-like shape (Fig. 9C and D) is a feature of these particles. This is clearly seen for particles lying at an angle to the shooting plane and a relatively high transparency of even large particles located parallel to the same plane. A similar morphology of Ni^0 particles characteristic of Ni/9YSZ, Ni/Zr873, and Ni/Zr703 was previously reported also for Ni/TiO_2 [70]. In addition to the raft-like shape, a cuboctahedral particle shape on Ni/amZr was observed (Fig. S5), also characteristic of Ni^0 [35,71].

The size distribution of Ni^0 particles (Fig. 9) strongly depends on the

Table 3
Hydrogen consumption and structural properties of Ni/ZrO_2.

Sample	Hydrogen consumption, mol.%			XRD results		TEM results		
	α-region 623–773 K	β-region 773–893 K	γ-region 893–1173 K	V_m, vol.%	d_{XRD}, nm	d_n, nm	d_s, nm	D_{Ni}, %
Ni/amZr	22	45	33	11	21.1	25	28	3,51
Ni/Zr703	37	56	7	89	17.1	41	59	1,71
Ni/Zr873	34	62	4	95	25.2	64	89	1,13
Ni/9YSZ	36	64	0	0	21.4	48	80	1,26

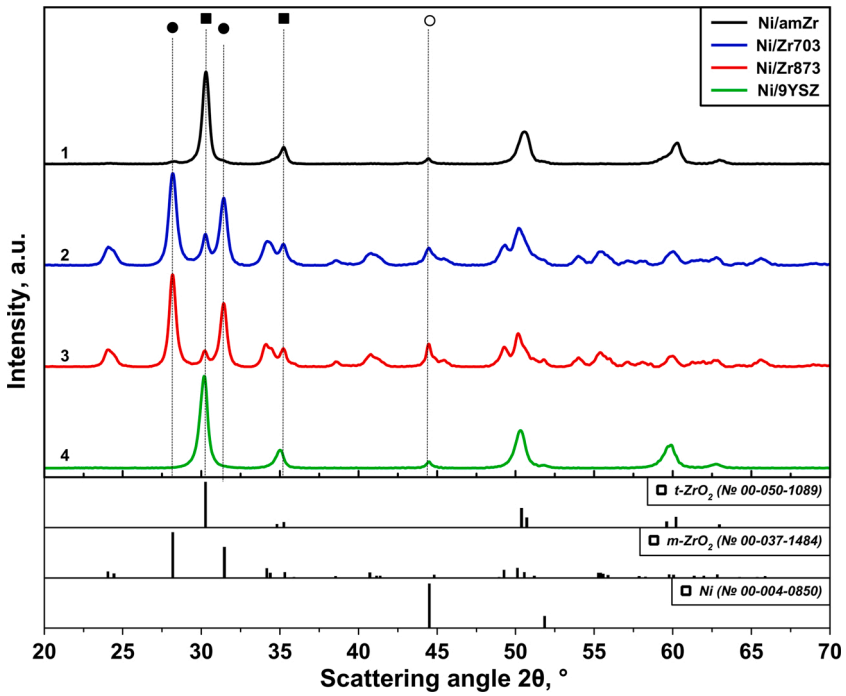

Fig. 7. XRD patterns of reduced samples: 1 – Ni/amZr; 2 – Ni/Zr703; 3 – Ni/Zr873; 4 – Ni/9YSZ (● – m-ZrO_2; ■ – t-ZrO_2; ○ – Ni^0).

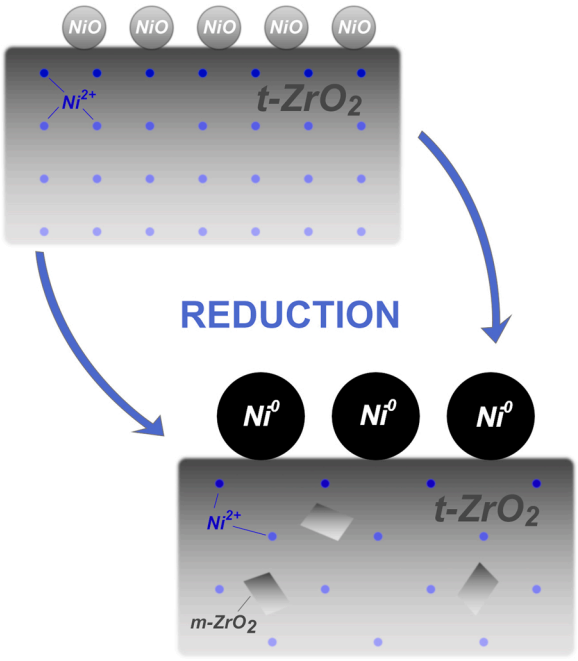

Fig. 8. A scheme of NiO/amZr transformations upon reduction.

initial form of ZrO_2. The particle size distribution of Ni^0 shifts towards larger values (d_n and d_s, Table 3) with an increase in the pretreatment temperature of ZrO_2. The narrowest distribution with a maximum at 25 nm is observed for Ni/amZr. The d_{XRD} value is quite different from the d_n value compared to XRD results. This is due to the raft-like morphology of Ni^0 particles, which is characterized by an increased size of the (111) plane. It should also be noted, that large Ni^0 particles could consist of several grains, which aggregates are not always distinguishable in the images. At the same time, the region of coherent scattering (the Scherrer equation) of the Ni^0 phase is equal to the particle size in the first approximation. The d_{XRD}, d_n, and d_s values for the Ni/amZr sample are the closest, which is due to the monomodal distribution.

Thus, the initial state of the zirconia support affects reducibility and the particle size of Ni^0 in Ni/ZrO_2. Reduction leads to an increase of the size of the deposited phase. The stabilizing effect of Ni^{2+} is retained after reduction in the samples based on amZr. The content of t-ZrO_2 content and the Ni^0 particle size (d_n и d_s) in the reduced samples increased in the order Ni/amZr < Ni/Zr703 < Ni/Zr873. The phase composition of thermostable supports (m-ZrO_2 for Zr873 and t-ZrO_2 for 9YSZ) effects the Ni^0 particles size, namely, an increased content of large Ni^0 particles is observed for a sample based on Zr873. It should be noted that further coarsening of Ni^0 particles could be expected with an increase in the zirconia pretreatment temperature and/or reduction of NiO/ZrO_2 due to more prominent bulk sintering of the support and surface mobility of Ni^0.

3.5. *Ni/ZrO_2 surface acidity*

Ammonia desorption profiles for Ni/ZrO_2 are shown in Fig. 10 while the calculation results (total acidity, acid sites density) are presented in Table 4.

All samples have three types of acid sites clearly distinguishable by the strength of ammonia adsorption: 386−563 K – weak, 563−803 K – medium, above 803 K – strong acid sites. The latter differ from the results of other studies by 70–100 K [11,24,25] which may be due to differences in the arrangement of thermocouples in the devices and surface properties of the samples. Ni/amZr, Ni/Zr703 and Ni/9YSZ have close values of total acidity (Table 4), and the sample based on m-ZrO_2 (Ni/Zr873) has the lowest total acidity. A larger difference is observed in the values of the surface density of acid sites. The latter was the highest for materials obtained from amZr and YSZ which phase composition after reduction is represented by t-ZtO_2 (Ni/amZr, Ni/9YSZ Fig. 7). The samples based on unstabilized t-ZrO_2/m-ZrO_2 and containing after reduction m-ZrO_2 (Ni/Zr703, Ni/Zr873) have the maximum and minimum values, respectively. An increase in the pretreatment temperature of the support (amZr < Zr703 < Zr873) leads to a decrease in the fraction of sites of the medium strength and an increase in the fraction of strong acid sites (Table 4). Introduction of Y^{3+} gives an increase in the fraction of medium strength centra, which agrees with the data of [25]. The Ni/amZr sample has, nevertheless, the highest content of these centers.

The obtained results show that the initial state of ZrO_2 influences acidity of Ni/ZrO_2 surface after introducing NiO and subsequently reducing it to Ni^0. According to the literature data [44,72–74], t-ZrO_2 has mainly Lewis acid sites (LAS), while m-ZrO_2 contains Lewis and Brønsted acid sites (BAS). LAS are the coordination unsaturated Zr^{3+}/Zr^{4+} (cus) atoms located either on vacancies or on crystal faces emerging at the surface [73,74]. Introduction of Y^{3+} results in an increase in the LAS amount on the t-ZrO_2 surface due to creation of

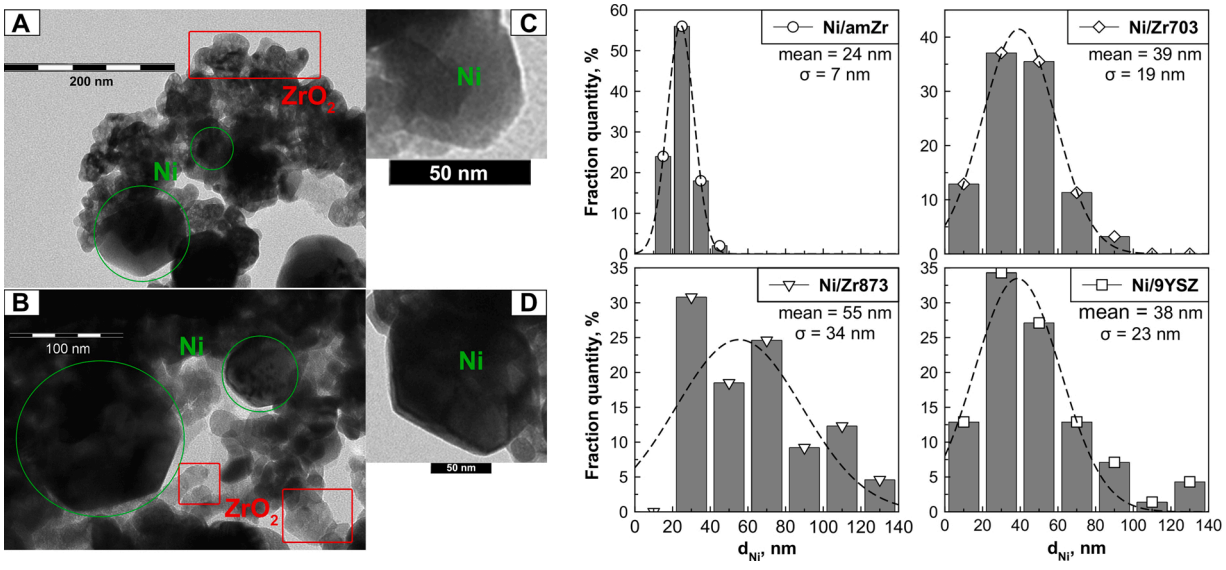

Fig. 9. TEM-images for Ni/9YSZ (A, C) and Ni/Zr873 (B, D) and Ni^0 particle size distributions for all samples.

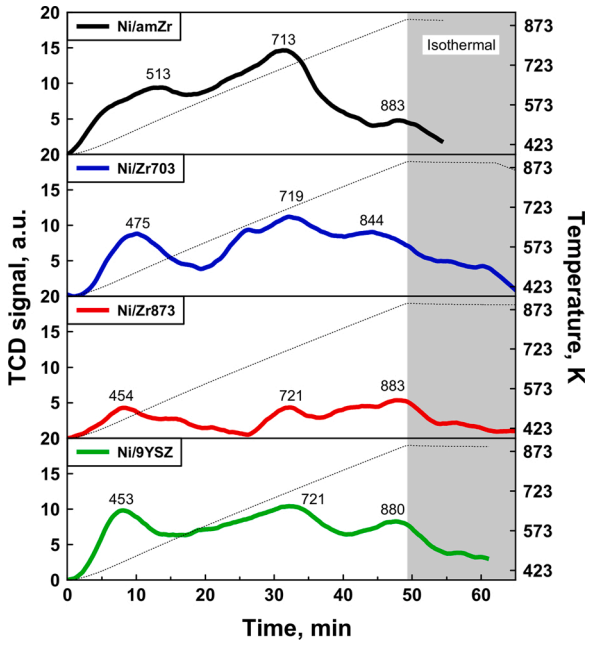

Fig. 10. NH_3-TPD profiles for Ni/ZrO_2.

additional vacancies that emerge on the surface [75], elevating the total acidity (Table 4). Apparently, Ni^{2+} has a similar effect (Ni/amZr sample) due to incomplete reduction of Ni^{2+} from a solid solution in ZrO_2 and an ability of divalent cations to create anionic vacancies in t-ZrO_2 [75]. An increased fraction of strong centers on the surface of Ni/Zr703 and Ni/Zr873, in which the phase composition is dominated by m-ZrO_2, agrees with the results in [73,76] reporting predominance of strong BAS (OH groups one- and three-coordinated to the zirconium ion) [73] and LAS [76] on the surface of m-ZrO_2. In the current work the surface density of the acid sites is significantly inferior to acidity of zirconia according to the literature (namely, 0.16–0.31 nm^{-2} in the this study and 1.7 nm^{-2} for t-ZrO_2 and 3.4 nm^{-2} for m-ZrO_2 [72]). Such differences may be due to differences in the synthesis methods for both ZrO_2 itself (especially m-ZrO_2) and introduction of NiO [38] as well as implementation of reduction. The effect of the surface acidity on the catalytic properties is discussed below.

3.6. Catalytic tests

3.6.1. Activity

High glycerol conversion and hydrogen yields were achieved at SRG temperatures above 823 K at WGFR exceeding 9:1 and atmospheric pressure in line with the thermodynamic data [77–79]. If similar conditions are used external or internal diffusion limitations can be anticipated for a catalyst exhibiting the highest activity. Therefore, influence of the residence time τ on X_{Ggas} was elucidated for Ni/9YSZ catalyst as an example. The values of all flow rates and calculation details are given in the Supplementary material (Table S1). Dependence of the glycerol conversion to gas (X_{Ggas}) vs τ is shown in Fig. S5. A sharp rise in X_{Ggas} with increasing residence time is observed up to τ of ca. 0.040 s, which indicates absence of external mass transfer limitations below this value. This conclusion is confirmed by the calculation of the Mears criterion for which the values 0.02–0.05 were obtained, being clearly lower than 0.15/n where n is the reaction order with respect to glycerol. The values of the reaction order for SRG were reported to be 0.2–0.5 [80]. At the same time based on the calculations of the Weisz-Prater criteria (Φ = 0.55–1.4 depending on the τ) the presence of internal mass transfer limitations cannot be completely ruled out. Subsequently, the following conditions were used to evaluate the initial activity of the catalysts from the TOF_{Gly} values: m_{cat} = 0.13 g, V_{liq} = 7.0 mL/h, $V(N_2)$ = 8 mL/min corresponding to τ = 0.021 s (WHSV = 160,000-170,000 h^{-1}).

The values of TOF_{Gly} for Ni/ZrO_2 are displayed in Fig. 11. The catalyst synthesized based on m-ZrO_2 (Ni/Zr873) has the highest initial activity among the samples based on unmodified ZrO_2. Moreover, Ni/Zr873 is more active than the catalyst based on thermostable t-ZrO_2 (Ni/9YSZ). A clear dependence of TOF_{Gly} on d_S visible in Fig. 11 indicates structure sensitivity of SRG in accordance with the literature data [16].

While in the literature the majority of studies report structure sensitivity in the range of 2–10 nm, there are also several publications where the changes in TOF were observed for much larger metal clusters. For example, in hydrogenation of acetone over copper catalysts the maximum in TOF was observed at ca. 110 nm [81]. Elevation of TOF up to the cluster size of Ru particles of 70 nm was seen for the Fischer-Tropsch synthesis [82]. In a series of silica and alumina supported platinum catalysts the highest TOF in NO oxidation was displayed by the material with the particle size of 27 nm [83]. For the latter reaction in another study the highest TOF was also noticed for platinum catalysts with a low metal dispersion, namely exhibiting the size of ca. 40 nm [84].

It was noted [85] that a comparison of catalytic results generated in different studies is possible if the same experimental conditions are used,

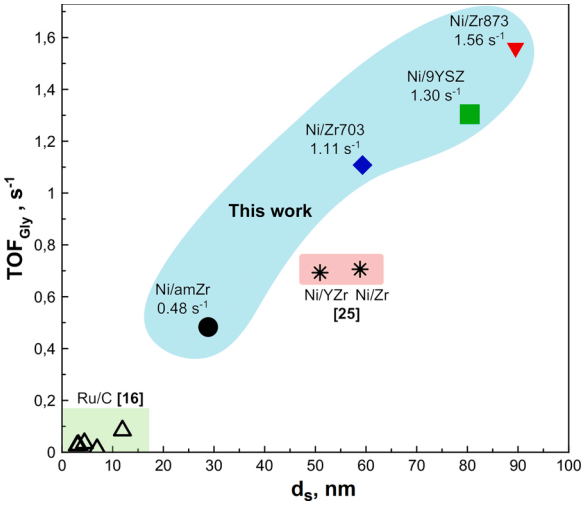

Fig. 11. Comparison TOF_{Gly} in glycerol steam reforming vs surface-weighted particle diameter over Ni/ZrO_2 obtained in this work with the data from [16, 25]. Conditions: m_{cat} = 0.13 g, V_{liq} = 7.0 mL/h, $V(N_2)$ = 8 mL/min.

Table 4
NH_3-TPD calculation results.

Sample	Ammonia desorption, mol. %			Total acidity, μmol/g	Acid sites density*, nm^{-2}
	Region 1 386–563 K	Region 2 563–803 K	Region 3 above 803 K		
Ni/amZr	28	58	14	121	0.21
Ni/Zr703	21	44	35	120	0.31
Ni/Zr873	26	31	44	50	0.16
Ni/9YSZ	26	45	29	120	0.28

* Acid sites density = (Total acidity [μmol/g] · $6.022 \cdot 10^{23}$ [mol^{-1}] · 10^{-24}) / SSA [m^2/g].

namely feed and reactor type, substrate concentration, temperature, the catalyst amount and loading, carrier gas flows and pressure. Most of the conditions used in this work are similar to those in [24,25,28] allowing a fair comparison. The TOF_{Gly} values calculated according to [25] for the catalysts supported on commercial ZrO_2 (Ni/Zr) and yttria-stabilized ZrO_2 (Ni/YZr) are also shown in Fig. 11. The size distributions of Ni^0 particles were used to calculate the values of d_c for the samples from [25] (59 nm for Ni/Zr and 51 nm for Ni/YZr). Activity of both catalysts is the same for a similar phase composition of the reduced samples, where t-ZrO_2 is dominating. Ni/9YSZ exhibited a two-fold higher initial activity compared to Ni/YZr catalyst reported in [25].

Thus, catalysts based on m-ZrO_2 (Ni/Zr873) and yttria-stabilized t-ZrO_2 (Ni/9YSZ) have the highest initial activity expressed by TOF_{Gly}.

3.6.2. Stability

Catalyst stability tests were carried out using either lower ($\tau = 0.021$, meeting the conditions of intrinsic activity tests) or elevated residence time ($\tau = 0.066$ s, $m_{cat} = 0.52$ g, $V_{liq} = 7.0$ mL/h, $V(N_2) = 30$ mL/min). The deactivation profiles of the samples are displayed in Fig. 12 for X_{Ggas} and $Y(H_2)$ values. The hydrogen yields are calculated using Eq. 8 without taking into account the stoichiometric coefficient of hydrogen in the SRG reaction equation equal to 7.

All tested catalysts showed the initial X_{Ggas} exceeding 85 mol.%. Ni/9YSZ catalyst exhibits the lowest conversion among all the samples at $\tau = 0.066$ s, however, conversion gradually increased up to TOS = 7 h (85.3–91.5 %). The induction period for Ni/9YSZ is also visible at $\tau = 0.021$ s in the first 30 min of the experiment. Other catalysts display a similar conversion of glycerol to gas at the same contact time for essentially the same TOS and at $\tau = 0.066$ s in the first 4 h. Subsequently their behavior diverged because of different deactivation rates. Time to get $X_{Ggas} = 75$ mol.% at $\tau = 0.066$ s and $X_{Ggas} = 50$ mol.% at $\tau = 0.021$ s increased in the order Ni/9YSZ < Ni/amZr < Ni/Zr703 < Ni/Zr873. Faster catalyst deactivation at shorter τ was also reported for SRM [86] and SRE [87].

The trends for $Y(H_2)$ vs TOS (Fig. 12B) are similar to those for X_{Ggas} at the corresponding contact time. A high hydrogen yield during the entire period of a stable operation at $\tau = 0.066$ s is characteristic for Ni/amZr, Ni/Zr703, and Ni/Zr873 catalysts. Ni/9YSZ displayed the highest hydrogen yield despite a lower X_{Ggas}, which is discussed in a more detail below.

Some indicators allowing a comparison of stability for various Ni/ZrO_2 materials are given in Table S2 and Fig. S6. The stable periods were observed at $\tau = 0.066$ s. The materials obtained from am-ZrO_2 and 9YSZ where t-ZrO_2 is predominant after reduction (i.e. Ni/amZr and Ni/9YSZ), exhibited the slowest deactivation similar to previous studies [20,24,25]. Both the conditions for obtaining ZrO_2 and thermal treatment can explain differences in the absolute values. Since in this work the materials were obtained from the same batch of ZrO_2 and thermally treated under the same conditions, the observed differences in the catalyst stability can be explained by the influence of the phase composition of the zirconia support.

Thus, the catalysts based on amZr (Ni/amZr) and yttria-stabilized t-ZrO_2 (Ni/9YSZ), where t-ZrO_2 is dominating in the phase composition after reduction, displayed the highest stability.

3.6.3. Selectivity for the major gas products

Differences in the catalytic behavior for studied materials being also dependent on the contact time are also evidenced in selectivity to the main gas-phase products (H_2, CO_2, CO in Fig. 13).

Hydrogen formed on Ni/amZr, Ni/Zr703 and Ni/9YSZ is further consumed in consecutive reactions. The different directions in the changes of selectivity for CO_2 and CO with deactivation are partly due to a decrease in the WGS reaction rate, which is most noticeable at $\tau = 0.021$ s. No apparent changes in $S(CO_2)$ and S(CO) with a drop in X_{Ggas} for Ni/Zr873 and Ni/Zr703 indicate participation of CO_2 and CO in parallel reactions. Carbon oxide can be formed and consumed in the following reactions: SRM, glycerol decomposition, DRM, coke gasification; WGS, CO hydrogenation and the Boudouard reaction. There was no significant decrease in $S(H_2)$ with a decreasing residence time which also affects the H_2/CO_2 ratio (Fig. S7). The amount of converted water, which is not taken into account in the calculation of $S(H_2)$ according to Eq. (9), may be the reason for such a result, along with S (H_2) > 100 % [88]. A decrease in the residence time has a negative effect on $S(CO_2)$ due to a decrease in CO conversion by the WGS reaction. A similar effect of τ was reported for SRE [33]. It should be noted that the samples, in which the phase composition after reduction is dominated by m-ZrO_2 (Ni/Zr703 and Ni/Zr873), are characterized by the largest difference in $S(CO_2)$ depending on τ at the same X_{Ggas}. Selectivity can be influenced by the internal diffusion of the reacting components, which impact is diminishing as the catalyst deactivates by coking.

It is also possible to distinguish two groups of samples with increased (Ni/Zr873 and Ni/9YSZ) and decreased (Ni/amZr and Ni/Zr703) selectivity for H_2 and, to a lesser extent, selectivity for CO_2. The reason for this difference is involvement of H_2 in hydrogenation reactions, which is discussed below.

3.6.4. Selectivity for gaseous and liquid byproducts

In addition to the main gas-phase products, formation of methane,

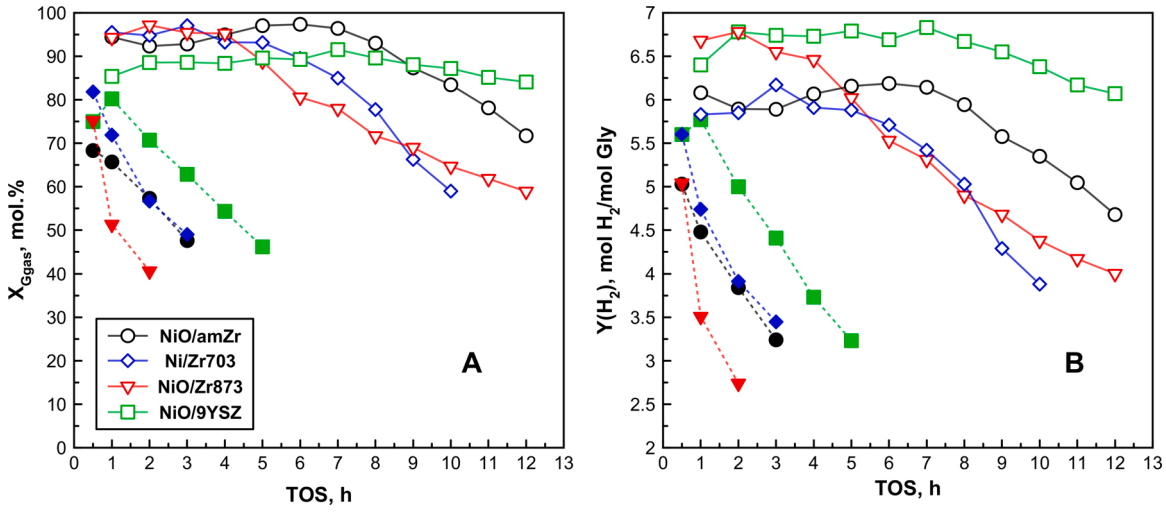

Fig. 12. Time-on-stream behavior in steam reforming of glycerol at different residence times: $\tau = 0.021$ s (- - -), $m_{cat} = 0.13$ g, $V_{liq} = 7.0$ mL/h, $V(N_2) = 8$ mL/min; $\tau = 0.066$ s (—), $m_{cat} = 0.52$ g, $V_{liq} = 7.0$ mL/h, $V(N_2) = 30$ mL/min. A) Conversion of glycerol to the gas products and B) H_2 yield.

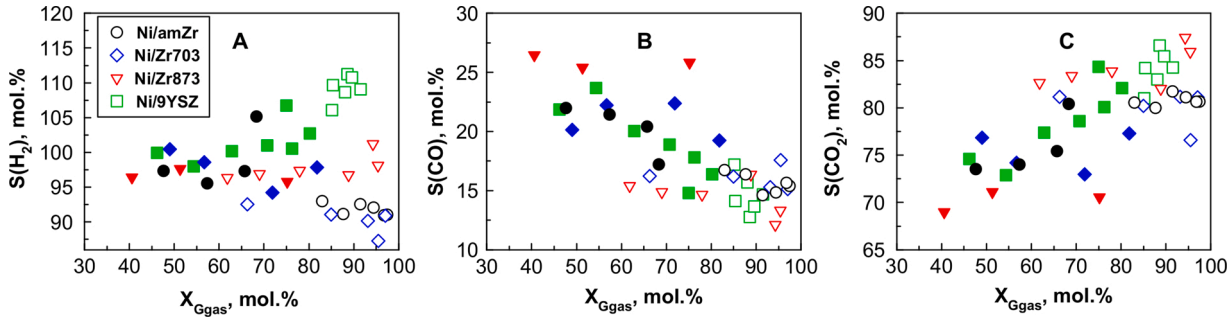

Fig. 13. Selectivity to the major gas products vs conversion at different contact times: $\tau = 0.021$ s (solid points), $m_{cat} = 0.13$ g, $V_{liq} = 7.0$ mL/h, $V(N_2) = 8$ mL/min; $\tau = 0.066$ s (open points), $m_{cat} = 0.52$ g, $V_{liq} = 7.0$ mL/h, $V(N_2) = 30$ mL/min.

ethane, ethylene, propane (Fig. 14), and liquid by-products (Fig. 15) was also observed.

Two groups of samples can be distinguished in terms of selectivity to methane S(CH_4) behavior vs a decrease in X_{Ggas}: Ni/9YSZ and Ni/Zr873 displayed an increase in S(CH_4), while for Ni/Zr703 and Ni/amZr an opposite dependence was observed. The methane selectivity for Ni/amZr873 and Ni/Zr703 approaches the values for Ni/Zr873 and Ni/9YSZ in the course of deactivation and a decrease in X_{Ggas}. The same pairs of samples demonstrate a decreased and an increased level of S(H_2), respectively, which indicates formation of CH_4 in the reactions requiring hydrogen.

Ethane, propane and ethylene are also found in the gas products (Fig. 14B–D). Selectivity to all these components decreased with an increase in X_{Ggas}, which is typical for intermediates in consecutive reactions. Such dependence along with a low selectivity to alkanes indicate steam reforming of ethane and propane at high glycerol conversion ($X_{Ggas} > 70$ mol.%). An increased selectivity to C_2H_4 and C_2H_6 was observed at a lower residence time $\tau = 0.021$ s, and after the beginning of a decrease in X_{Ggas} at $\tau = 0.066$ s. Formation of propane was visible mainly at $\tau = 0.021$ s, concomitant with accelerated deactivation. In this case, selectivity to C_2H_4, C_2H_6, and C_3H_8 was not affected.

HPLC analysis of the liquid by-products accumulated over 12 h of testing at $\tau = 0.066$ s (Fig. 15) shows a difference in the product composition and the amount of formed liquid by-products depending on the catalyst. The concentration of the liquid products increases in the same order as the catalyst stable operation time: Ni/9YSZ < Ni/amZr < Ni/Zr873. Based on HPLC, the carbon balance closure for Ni/amZr, Ni/Zr873 and Ni/9YSZ was 96.5, 93 and 90 % respectively. Interestingly several condensation products namely mannitol, erythritol, 2,3-butanediol were obtained. Formation of such products is characteristic of glycerol APR [7] and was not previously mentioned as SRG products. The mannitol content decreased in the order Ni/9YSZ < Ni/amZr < Ni/Zr873 samples. Apparently, mannitol is formed during hydrogenation of glucose which is a product of aldol condensation of 1,3-dihydroxyacetone or glyceraldehyde. Erythritol is detected only in the liquid phase products for Ni/Zr873. Erythrose and glycoaldehyde can be formed by the retro-aldol condensation of glucose. In turn, each of these two components can undergo hydrogenation to form erythritol and ethylene glycol, respectively. Ni/Zr873 was also characterized by the highest amounts of pyruvaldehyde, hydroxyacetone, ethylene glycol, ethanol and/or allyl alcohol, while the contribution of 2,3-butanediol,

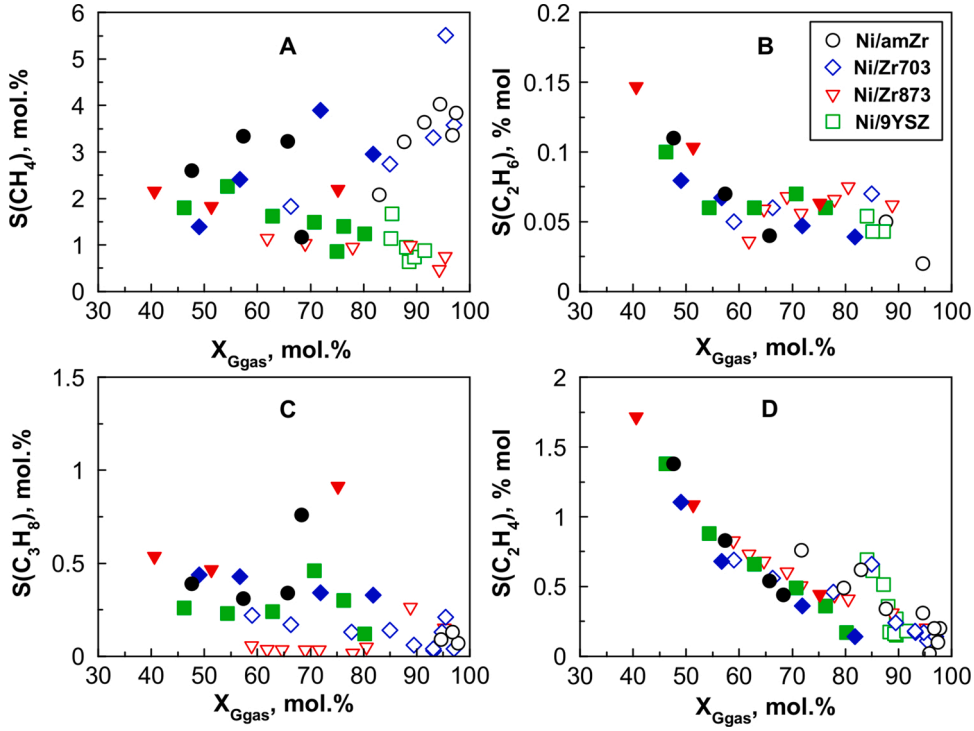

Fig. 14. Selectivity to C_1-C_3 hydrocarbons vs conversion at different contact times $\tau = 0.021$ s (solid points), $m_{cat} = 0.13$ g, $V_{liq} = 7.0$ mL/h, $V(N_2) = 8$ mL/min; $\tau = 0.066$ s (open points), $m_{cat} = 0.52$ g, $V_{liq} = 7.0$ mL/h, $V(N_2) = 30$ mL/min.

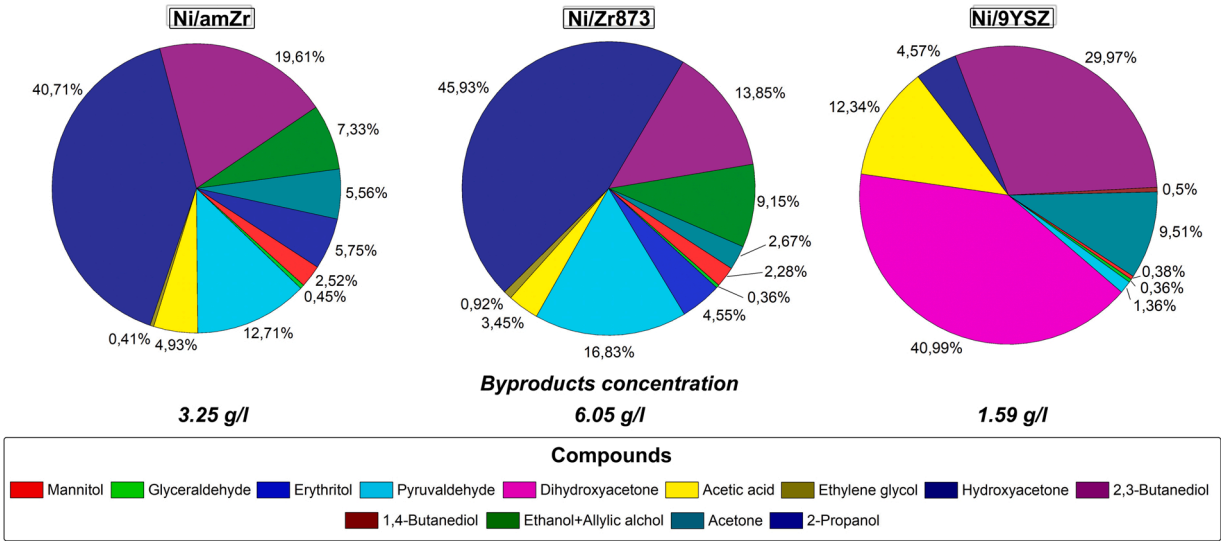

Fig. 15. HPLC analysis results of the liquid products accumulated over 12 h of catalytic tests at $\tau = 0.066$ s.

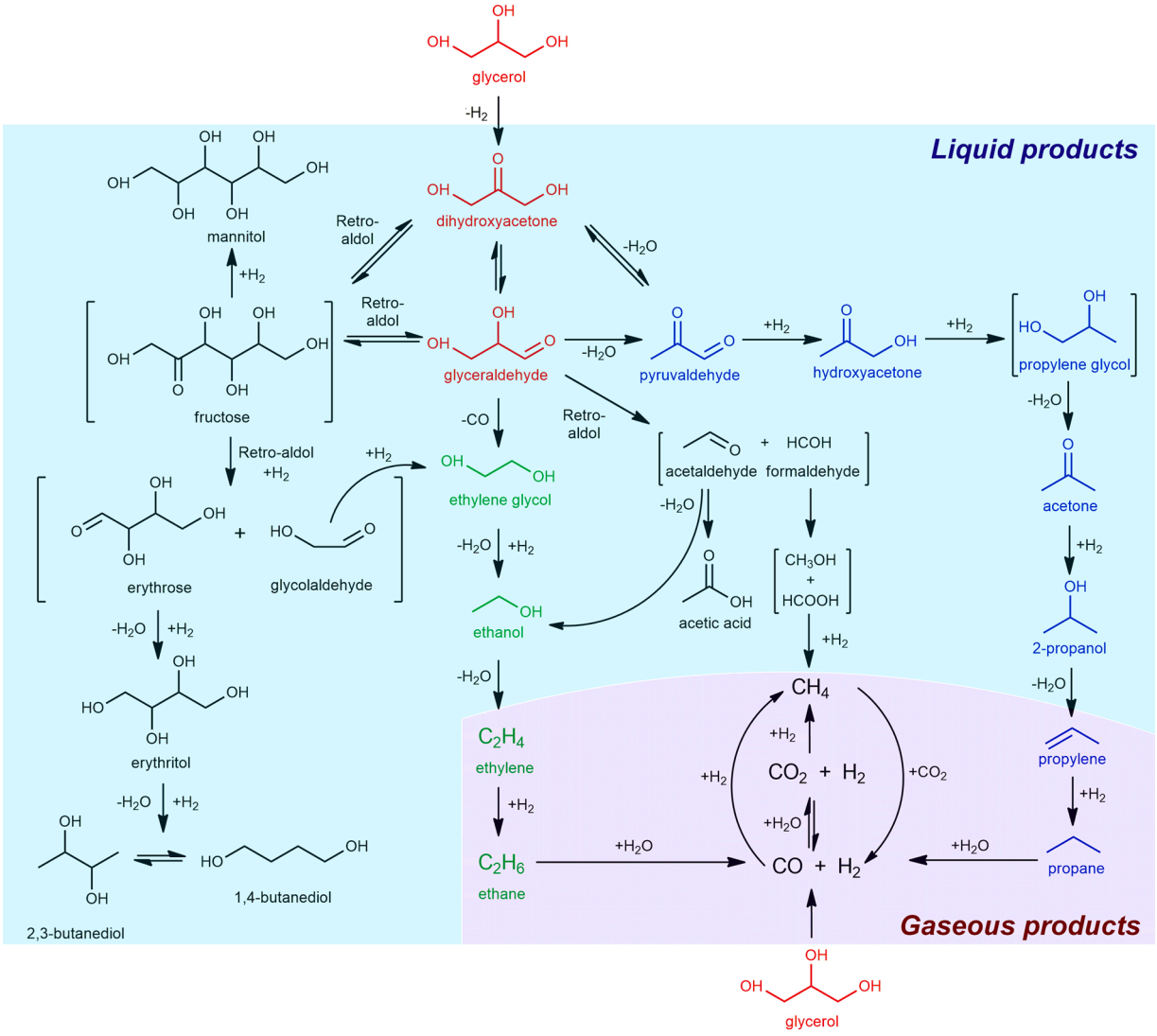

Fig. 16. The reaction network in SRG with the products not detected by HPLC given square brackets.

acetone, and acetic acid was the lowest. The highest amounts of 1, 3-dihydroxyacetone, which is the primary product of glycerol dehydrogenation, were observed in the liquid products in the case of Ni/9YSZ catalyst. The same catalyst gave also 2,3-butanediol, acetic acid and acetone. It is also important to mention presence of 2-propanol among the liquid-phase products for Ni/amZr.

It follows from the HPLC and GC results that formation of methane, ethane, propane, and ethylene can be associated with transformations of the glycerol decomposition products. It was stated in [85] that there are three routes of methane formation in the glycerol APR: methanation of CO, hydrogenation of methanol, or hydrogenation of a terminal C–CH_3 bond. The values of $S(H_2)$ and $S(CO_2)$ point out on occurrence of the Sabatier reaction. In addition, CO methanation cannot be excluded as this reaction happens at 623 K in the presence of a Ni catalyst. Formation of CH_4 can also occur as a result of hydrogenation and/or steam reforming of methanol which is formed by disproportionation of formaldehyde. The latter, in turn, is formed by the retro-aldol condensation of glyceraldehyde. Absence of formaldehyde, acetaldehyde, methanol, and at the same time presence of acetic acid, indicates participation of glycerol decomposition products in the formation of CH_4. Dependencies of $S(CH_4)$ vs X_{Ggas} (Fig. 14) correspond to consecutive reactions, in which CH_4 is an intermediate product, being consumed further during decomposition or SRM. Consequently, the rates of reactions consuming CH_4 decrease during deactivation of Ni/Z873 and Ni/9YSZ. At the same time, for Ni/Zr703 and Ni/amZr, the rates of these reactions increased with a decrease in X_{Ggas}. Absence of the corresponding changes in S (CO_2) and S(CO) with a decrease in $S(CH_4)$ by 4–5 % indicates occurrence of the subsequent SRM on Ni/Zr703 and Ni/amZr.

Analysis of the gas- and liquid-phase products indicates that ethane, ethylene, and propane originate from dehydration (followed by hydrogenation giving alkanes) of ethanol and 2-propanol, respectively. The scheme of the main reactions is shown in Fig. 16 based on the obtained results and literature data [10,13,89].

Comparison of the investigated catalysts at X_{Ggas} = 50–60 mol.% and τ = 0.021 s (Table S3) shows that selectivity to hydrogen, methane and carbon dioxide, while selectivity to carbon monoxide increases in the following order: Ni/amZr < Ni/Zr703 < Ni/Zr873 in line with a decrease of the t-ZrO_2 phase content in the reduced samples. The Ni-catalyst based on t-ZrO_2 (Ni/amZr) demonstrated elevated values of S (CO_2) and $Y(H_2)$, and lower S(CO) and $S(CH_4)$ in comparison with the catalyst based on m-ZrO_2 (Ni/Zr873), in agreement with the data for unmodified ZrO_2 [28]. Ni-catalyst based on yttria-stabilized t-ZrO_2 (Ni/9YSZ) shows higher $S(H_2)$, $S(CO_2)$, and also lower $S(CH_4)$ than Ni/amZr based on unstabilized t-ZrO_2. A similar result was obtained in [25] for yttria-stabilized and unstabilized t-ZrO_2. In [25,28] an opposite behavior of selectivity to methane during deactivation was observed. Changes in selectivity to methane $S(CH_4)$ depend on the initial form of the zirconia support, as shown in Fig. 14 and discussed below. At the same time, a low content of C_2H_4 in the gas-phase products was reported in [25]. Fig. 14 illustrates however, that $S(C_2H_4)$ reaches 1.7 % and increases with deactivation. According to the current work, ethane and propane are also formed in SRG, which was not reported in [25,28].

The following conclusions can be drawn from the results of the catalytic tests. Catalysts based on thermally stable supports of tetragonal and monoclinic modification (i.e. Ni/9YSZ and Ni/Zr873) have the highest initial activity (TOF_{Gly}). Ni/amZr and Ni/9YSZ catalysts obtained from amorphous zirconia and yttria-stabilized zirconia, with the main contribution of t-ZrO_2 in the phase composition, exhibited the best stability. A decrease in selectivity to hydrogen, methane and carbon dioxide, and an increase in the content of the glycerol decomposition products can be related to an increase in the fraction of m-ZrO_2 (Ni/amZr < Ni/Zr703 < Ni/Zr873) in the reduced samples. The amount of the liquid by-products and transformations of the latter to gaseous alkanes correlate with catalyst deactivation. Formation of CH_4 can occur both by methanation of CO_2 and/or CO, as well as by transformations of glycerol decomposition products. Further discussion about the reasons for different catalytic behaviour requires evaluation of the properties of the spent catalysts.

3.7. Spent catalysts

There are various reasons and mechanisms for deactivation of the steam reforming catalysts [5,90–92] including fouling and thermal sintering of both the support and the active phase. The type of coke is determined by the feedstock, nature of the catalyst surface and the operation conditions, while resistance to sintering depends on the ZrO_2 support thermal stability.

The DTA curves of the catalysts used at the residence time of 0.066 s are shown in Fig. 17. The deposits formed during the catalytic tests were burnt out in the temperature range of 713–963 K. The coke amount (Table 5) increased in the order Ni/Zr873 < Ni/9YSZ < Ni/Zr703 < Ni/amZr. The pore volume decreases in the same order when comparing spent samples with the reduced ones. The value of the residual conversion (X_{Ggas} (10 h), Table 5) does not correlate with the total amount of coke formed even if the amounts of deposits were significantly different.

As noted in the Introduction, the type of coke deposits has a larger impact on the catalyst stability than the coke amount. Various options for discussing coke burnup curves are discussed in [38,93–96]. There are two areas of coke burnout, one is related to amorphous coke (up to 823–873 K), while the second corresponds to the graphite-like and filamentary coke (above 873 K). Analysis of the TG curves of the spent catalysts (Table 5) allows to rank the catalysts in terms of the fraction of graphite (C_c) and/or filamentous coke (C_v) increasing in the order Ni/amZr < Ni/Zr703 < Ni/Zr873 < Ni/9YSZ.

During SRG sintering occurred as follows from the XRD results for the reduced (Table 3) and spent catalysts (Table 5, Fig. S8). The content of m-ZrO_2 increased in the samples based on non-promoted ZrO_2: up to 49 vol.% for Ni/amZr and up to 99 vol.% m-ZrO_2 for Ni/Zr703. The region of the coherent scattering Ni^0 (d_{XRD}) has increased mainly to 26–28 nm with the largest changes in d_{XRD} observed for Ni/Zr703 and Ni/amZr. While in general a decrease in the pore volume can be ascribed to sintering and coking with different contribution, such decrease for Ni/9YSZ and Ni/Zr873 is explained by coking as no sintering of the supports after SRG was recorded. In the diffraction patterns of the spent catalysts (Fig. S8) there is a weak reflection at 26.32° (2θ), corresponding to graphite. This further confirms thermal analysis results pointing out on the presence of graphite-like deposits.

Division of samples into two groups (Ni/amZr, Ni/Zr703 and Ni/Zr873, Ni/9YSZ) according to Figs. 13 and 14 holds also the spent

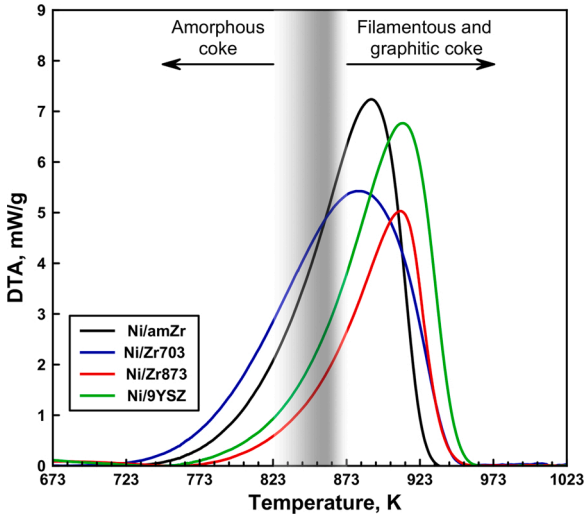

Fig. 17. DTA-curves of the spent catalysts.

Table 5
Characteristics of the spent catalysts.

Sample	X_{Ggas} (10 h), mol. %	TG results			XRD results		Loss of the pore volume [a], vol.%
		Coke amount, g coke/g cat.	Amorphous coke, wt. %	Filamentous and graphitic coke, wt.%	V_m, vol. %	d_{XRD}, nm	
Ni/amZr	83	0.22	53	47	60	26.1	32
Ni/Zr703	59	0.20	54	46	99	28.3	45
Ni/Zr873	65	0.11	31	69	99	27.5	54
Ni/9YSZ	87	0.17	26	74	0	20.1	50

[a] $(V_p(spent)/V_p(reduced))\cdot.100$ %.

catalysts (Fig. 17). More CH_4 and total coke were observed on Ni/amZr and Ni/Zr703 while there was less graphitic coke formed. The opposite results were displayed by Ni/Zr873 and Ni/9YSZ. Methane decomposition to C and H_2 is one of the main reactions of coke formation, as well as one of the paths for methane consumption apart from SRM. It is known that catalyst coking occurs when the rate of coke deposition exceeds the rate of its gasification [91,92,96]. The primary forms of coke (C_α and C_β) generated during decomposition of CH_4 and CO are transformed into a graphite-like species at a high process temperature and a large amount of accumulated coke. Apparently, in the first hours of Ni/amZr and Ni/Zr703 testing, the rates of CH_4 formation and its further conversion with steam exceeded the rate of coke formation, as evidenced by an increased selectivity to methane $S(CH_4)$. Hydrogenation and gasification of the primary forms of coke could also take place, preventing their rapid accumulation and further transformations into a graphite-like form. The opposite was observed for Ni/Zr873 and Ni/9YSZ, exhibiting low $S(CH_4)$ from the very beginning of testing and a high fraction of graphite-like coke.

Thus, with an increase in the fraction of m-ZrO_2 in the initial reduced sample (Ni/amZr < Ni/Zr703 < Ni/Zr873) the total coke content decreases, the fraction of graphite-like coke increases, and the pore volume decreases. The most stable Ni/amZr catalyst based on unpromoted ZrO_2 has the highest total coke content, the lowest C_c content, a residual amount of t-ZrO_2 reaching 40 %, and the lowest decrease of the pore volume. An average amount of coke, an increased fraction of C_c, and a substantial decrease in the pore volume along with a stable support phase composition and the particle size of metallic nickel are characteristic for Ni/9YSZ, displaying the highest stability among all catalysts.

3.8. Relationship between physicochemical and catalytic properties

The obtained results show that the initial state of ZrO_2 affects synthesis of the final catalysts. Furthermore, investigation of the effect of the initial treatment temperature of unpromoted ZrO_2 (amZr – Zr703 – Zr873) and the phase composition of ZrO_2 confirmed that there is no influence of Ni^{2+} on the formation of ZrO_2 (Zr873 and 9YSZ). The most important catalyst characteristic, which is influenced by the initial state of the support, is the size of the Ni^0 particles formed after NiO reduction. Since the same test conditions were used in this work, the observed differences in the catalytic properties can be ascribed to differences in the size of Ni^0 particles [96].

An increase in the size of Ni^0 particles elevating the zirconia pretreatment temperature determines the initial catalytic activity in the order Ni/amZr < Ni/Zr703 < Ni/Zr873. The differences in selectivity for CH_4 are apparently due to the presence of an increased fraction of small particles of Ni^0 (d_{TEM} < 40 nm) in Ni/amZr and Ni/Zr703 in comparison with Ni/Zr873, because such particles afforded higher $S(CH_4)$ during methanation of CO/CO_2 [65,97]. A rapid decline in $S(CH_4)$ for Ni/amZr and Ni/Zr703 is due to agglomeration of Ni^0 particles during deactivation [98], which follows from XRD data (Tables 3 and 5). The character of the $S(CH_4)$ vs X_{Ggas} dependence for Ni/amZr and Ni/Zr703 shows more methane consumption at lower X_{Ggas}, apparently, in the decomposition reaction giving coke. Since the rate of coke accumulation directly depends on the particle size of Ni^0 [41,99], coke is formed on Ni/amZr and Ni/Zr703 more slowly and with lower crystallinity than on Ni/Zr873 which possess a larger initial size of metallic nickel particles. Formation of the graphite-like coke on Ni/Zr873 from the beginning of the catalytic test, apparently, led to encapsulation of Ni^0 particles and rapid deactivation. This is facilitated by the low degree of metal-support interactions (MSI) Ni^0 with m-ZrO_2 [41,99], which decreases in the order Ni/amZr > Ni/Zr703 > Ni/Zr873 (Fig. 6).

The surface acidity can contribute to coking of the catalyst, namely with an increase in the fraction of medium acid sites and subsequently a decrease in the fraction of strong acid sites (Table 4), the total coke content increases (Table 5). However, as noted in [25], a larger number of strong centers promotes formation of a larger number of coke precursor compounds. Such a difference can be explained by the influence of not only the strength, but also the type of acid sites, e.g. BAS promote the coke formation [44]. It is also worth noting a tendency for the total coke content to increase with an increase in total acidity. The lowest coke content is characteristic for the least acidic Ni/Zr873. The same catalyst exhibited the lowest selectivity to propane (Fig. 14C) indicating that the acid sites are required for efficient dehydration reactions, which are a part of the reaction route from glycerol to propane.

Comparison of Ni/9YSZ and Ni/Zr873 based on thermostable supports of various modifications (t-ZrO_2 and m-ZrO_2, respectively) shows that the size of Ni^0 particles, initial activity, and coke graphitization are similar. The increased d_s (Table 3) on the surface of both samples appears to be due to the decreased MSI. However, the catalyst based on yttria-stabilized t-ZrO_2 showed better stability in SRG, the $Y(H_2)$ yield, selectivity for the main gas-phase products and the total amount of coke. Moreover, the same catalyst displayed a smaller amount of liquid by-products and a degree of their conversion. Ni/9YSZ is characterized by deactivation through coking rather than sintering which was not seen for either the support or Ni^0. High stability during formation of graphite-like coke is apparently associated with an increased oxygen storage capacity and the structure of yttria-modified ZrO_2 containing defects in comparison with m-ZrO_2 (Zr873), as is noted in several studies [25,65]. The presence of oxygen vacancies improved coke gasification, preventing encapsulation of nickel particles. A special feature of Ni/amZr is that Ni^{2+} acts as a stabilizer of t-ZrO_2 (similar to Y^{3+}) and a source of the active phase (Ni^0). The residual Ni^{2+} dissolved in t-ZrO_2 prevented the complete transition t-ZrO_2 → m-ZrO_2, and strong sintering of the support and Ni^0. The escape of Ni^{2+} from the support during NiO/amZr reduction can lead to formation of defects on the ZrO_2 surface, facilitating coke gasification.

Brønsted acid sites (surface OH-groups) and surface defects can contribute to the high initial activity of Ni/9YSZ and Ni/Zr873 (Section 3.5 and 3.6.1). It was shown in [39] that Au/ZrO_2 catalyst based on m-ZrO_2 is more active than a catalyst based on unstabilized t-ZrO_2 in low-temperature WGS. The authors of [39] explain the difference in activity by the influence of surface acidic OH-groups of m-ZrO_2 on the strength of CO adsorption, as well as its increased surface defectiveness compared to unstabilized t-ZrO_2. YSZ also has defective positions on the

surface, which are the coordination unsaturated Zr^{3+}/Zr^{4+}. The presence of surface defects leads to additional activation of H_2O molecules and their involvement in the catalytic cycle.

4. Conclusion

For the first time the influence of the initial state of ZrO_2 support (amorphous $ZrO_2{\cdot}nH_2O$, t-ZrO_2, m-ZrO_2, YSZ) obtained from a single precipitation product on the genesis of the nickel-zirconium catalysts, their activity, stability and selectivity in the steam reforming of glycerol was studied. Changes in the initial phase composition of the support due to variations in the treatment temperature of $ZrO_2{\cdot}nH_2O$ significantly affect the main characteristics of the catalyst, i.e. the size and shape of Ni^0 particles. The largest size of Ni^0 is typical for thermally stabilized supports based on m-ZrO_2 and YSZ.

The catalyst based on m-ZrO_2, along with YSZ, have higher initial values of the turnover frequency (1.3–1.6 s^{-1}) compared to the catalyst based on am-ZrO_2 (0.5 s^{-1}) which indicates a possibility of obtaining promising reforming catalyst using monoclinic zirconia as the support. The smallest amount of CH_4 during methanol or/and CO/CO_2 hydrogenation is formed for catalysts based on m-ZrO_2 and YSZ with an increased content of large Ni^0 particles (> 60 nm). For the first time mannitol and erythritol were found in the liquid by-products formed during glyceraldehyde/dihydroxyacetone aldol condensation, which also explains formation of butanediols. The transformation rate of the condensed products directly depends on the level of catalyst deactivation. It has been established, that the most stable catalysts are characterized by an increased residual content of t-ZrO_2 and minor sintering of Ni^0, which can be a result of a stabilizing effect of Ni^{2+} on t-ZrO_2.

The obtained results show the importance of choosing the initial form of the zirconia support to ensure high activity, stability and selectivity of Ni/ZrO_2 catalysts in steam reforming of glycerol.

Authors statement

Sh.O. Omarov Investigation; Data curation; Writing - original draft;
D.A: Sladkovkiy Investigation; Data curation;
K.D. Martinson, Methodology;
Markus Peurla Data curation;
Atte Aho, Data curation; Methodology;
Dmitry Yu. Murzin Conceptualization; Supervision; Writing - review & editing
V.I. Popkov, Conceptualization; Funding acquisition; Supervision

Declaration of Competing Interest

The authors report no competing financial interests.

Appendix A. Supplementary data

Supplementary material related to this article can be found, in the online version, at doi:https://doi.org/10.1016/j.apcata.2021.118098.

References

[1] A. Iulianelli, S. Liguori, J. Wilcox, A. Basile, Catal. Rev. 58 (1) (2016) 1–35.
[2] R. Estevez, L. Aguado-Deblas, F.M. Bautista, D. Luna, C. Luna, J. Calero, A. Posadillo, A.A. Romero, Catalysts 9 (12) (2019) 1033–1070.
[3] J.M. Silva, M.A. Soria, L.M. Madeira, Renew. Sust. Energy Rev. 42 (2015) 1187–1213.
[4] N.D. Charisiou, K. Polychronopoulou, A. Asif, M.A. Goula, Surf. Coat. Technol. 352 (2018) 92–111.
[5] N.A. Roslan, S.Z. Abidin, A. Ideris, D.V.N. Vo, Int. J. Hydrogen Energy 45 (36) (2020) 18466–18489.
[6] N.N.M. Arif, D.V.N. Vo, M.T. Azizan, S.Z. Abidin, Bull. Chem. React. Eng. Catal. 11 (2) (2016) 200–209.
[7] L.I. Godina, A.V. Tokarev, I.L. Simakova, P. Mäki-Arvela, E. Kortesmäki, J. Gläsel, L. Kronberg, B. Etzold, D.Yu. Murzin, Catal. Today 301 (2018) 78–89.
[8] A. Morales-Marín, J.L. Ayastuy, U. Iriarte-Velasco, M.A. Gutiérrez-Ortiz, Appl. Catal. B 244 (2019) 931–945.
[9] A. Seretis, P. Tsiakaras, Renew. Energy 85 (2016) 1116–1126.
[10] M.A. Goula, N.D. Charisiou, K.N. Papageridis, G. Siakavelas, Chin. J. Catal. 37 (11) (2016) 1949–1965.
[11] N.D. Charisiou, K.N. Papageridis, G. Siakavelas, L. Tzounis, K. Kousi, M.A. Baker, S. J. Hinder, V. Sebastian, K. Polychronopoulou, M.A. Goula, Top. Catal. 60 (2017) 1226–1250.
[12] J.R. Rostrup-Nielsen, T. Rostrup-Nielsen, CATTECH 6 (2002) 150–159.
[13] K.N. Papageridis, G.S. Nikolaos, D. Charisiou, D.G. Avraam, L. Tzounis, K. Kousi, M.A. Goula, Fuel Proc. Technol. 152 (2016) 156–175.
[14] M. Konsolakis, Z. Ioakimidis, T. Kraia, G.E. Marnellos, Catalysts 6 (3) (2016) 39–65.
[15] M. Greluk, M. Rotko, G. Słowik, S. Turczyniak-Surdacka, J. Energy Inst. 92 (2) (2019) 222–238.
[16] E. Gallegos-Suárez, A. Guerrero-Ruiz, I. Rodríguez-Ramos, Carbon 96 (2016) 578–587.
[17] J.P. da S.Q. Menezes, R.L. Manfro, M.M.V.M. Souza, Int. J. Hydrogen Energy 43 (32) (2018) 15064–15082.
[18] C.K. Cheng, S.Y. Foo, A.A. Adesina, Catal. Today 178 (1) (2011) 25–33.
[19] M.M. Pakulska, C.M. Grgicak, J.B. Giorgi, Appl. Catal. A 332 (1) (2007) 124–129.
[20] I. Rossetti, A. Gallo, V. Dal Santo, C.L. Bianchi, V. Nichele, M. Signoretto, E. Finocchio, G. Ramis, A. Di Michele, ChemCatChem 5 (2013) 294–306.
[21] R. Manfro, N.F.P. Ribeiro, M.M.V.M. Souza, Catal. Sustain. Energy 1 (2013) 60–70.
[22] Y. Li, L. Zhang, Z. Zhang, Q. Liu, S. Zhang, Q. Liu, G. Hu, Y. Wang, X. Hu, Appl. Catal. A 584 (2019), 117162.
[23] S. Adhikari, S.D. Fernando, S.D. Filip To, R.M. Brick, P.H. Steele, A. Haryanto, Energy Fuels 22 (2) (2008) 1220–1226.
[24] N.D. Charisiou, K.N. Papageridis, G. Siakavelas, V. Sebastian, S.J. Hinder, M. A. Baker, K. Polychronopoulou, M.A. Goula, Catal. Today 319 (2019) 206–219.
[25] N.D. Charisiou, G. Siakavelas, L. Tzounis, B. Dou, V. Sebastian, S.J. Hinder, M. A. Baker, K. Polychronopoulou, M.A. Goula, Int. J. Hydrogen Energy 45 (17) (2020) 10442–10460.
[26] B. Jiang, L. Li, Z. Bian, Z. Li, Y. Sun, Z. Sun, D. Tang, S. Kawi, B. Dou, M.A. Goula, Int. J. Hydrogen Energy 43 (29) (2018) 13200–13211.
[27] S. Kitamura, T. Su-enaga, N. Ikenaga, T. Miyake, T. Suzuki, Catal. Lett. 141 (2011) 895–905.
[28] E. Dahdah, J. Estephane, C. Gennequin, A. Aboukaïs, E. Abi-Aad, S. Aouad, Int. J. Hydrogen Energy 45 (7) (2020) 4457–4467.
[29] J.-M. Wei, B.-Q. Xu, J.-L. Li, Z.-X. Cheng, Q.-M. Zhu, Appl. Catal. A 196 (2) (2000) L167–L174.
[30] I. Rossetti, C. Biffi, C.L. Bianchi, V. Nichele, M. Signoretto, F. Menegazzo, E. Finocchio, G. Ramis, A. Di Michele, Appl. Catal. B 117-118 (2012) 384–396.
[31] V. Nichele, M. Signoretto, F. Pinna, F. Menegazzo, I. Rossetti, G. Cruciani, G. Cerrato, A. Di Michele, Appl. Catal. B 150-151 (2014) 12–20.
[32] S. Li, C. Zhang, Z. Huang, G. Wu, J. Gong, Chem. Commun. 49 (2013) 4226–4228.
[33] S. Li, M. Li, C. Zhang, S. Wang, X. Ma, J. Gong, Int. J. Hydrogen Energy 37 (3) (2012) 2940–2949.
[34] S. Li, C. Zhang, P. Zhang, G. Wu, X. Ma, J. Gong, Phys. Chem. Chem. Phys. 14 (2012) 4066–4069.
[35] L. Azancot, L.F. Bobadilla, J.L. Santos, J.M. Córdoba, M.A. Centeno, J.A. Odriozola, Int. J. Hydrogen Energy 44 (36) (2019) 19827–19840.
[36] Y. Matsumura, T. Nakamori, Appl. Catal. A 258 (1) (2004) 107–114.
[37] J.G. Jakobsen, T.L. Jørgensen, I. Chorkendorff, J. Sehested, Appl. Catal. A 377 (1-2) (2010) 158–166.
[38] Q. Zhao, Y. Wang, Y. Wang, L. Li, W. Zeng, G. Li, C. Hu, Int. J. Hydrogen Energy 45 (2020) 14281–14292.
[39] J. Li, J. Chen, W. Song, J. Liu, W. Shen, Appl. Catal. A 334 (2008) 321–329.
[40] E.M. Albuquerque, L.E.P. Borges, M.A. Fraga, C. Sievers, ChemCatChem 9 (14) (2017) 2675–2683.
[41] X. Zhang, M. Zhang, J. Zhang, Q. Zhang, N. Tsubaki, Y. Tan, Y. Han, Int. J. Hydrogen Energy 44 (33) (2019) 17887–17899.
[42] G.K. Chuah, S. Jaenicke, S.A. Cheong, K.S. Chan, Appl. Catal. A 145 (1-2) (1996) 267–284.
[43] G. Deshmane, Y.G. Adewuyi, Microporous Mesoporous Mater. 148 (1) (2012) 88–100.
[44] Sh.O. Omarov, E.A. Vlasov, D.A. Sladkovskiy, K.V. Semikin, A.N. Matveyeva, S. P. Fedorov, G.V. Oganesyan, D.Yu. Murzin, Appl. Catal. B 230 (2018) 246–259.
[45] A.N. Matveyeva, N.A. Zaitseva, P. Mäki-Arvela, A. Aho, A.K. Bachina, S.P. Fedorov, D.Yu. Murzin, N.A. Pakhomov, Ind. Eng. Chem. Res. 57 (3) (2018) 927–938.
[46] H. Toraya, M. Yoshimura, S. Somiya, J. Am. Chem. Soc. 67 (6) (1984) 119–121.
[47] D.Yu. Murzin, T. Salmi, Catalytic kinetics. Chemistry and Engineering, 2nd edition, Elsevier, 2016.
[48] T. Itoh, J. Mater. Sci. Lett. 4 (1985) 1029–1032.
[49] P.D.L. Mercera, J.G. Van Ommen, E.B.M. Doesburg, A.J. Burggraaf, J.R.H. Ross, Appl. Catal. 57 (1) (1990) 127–148.
[50] D. Tichit, D. El Alami, F. Figueras, Appl. Catal. A 145 (1-2) (1996) 195–210.
[51] R.C. Garvie, M.F. Goss, J. Mater. Sci. 21 (4) (1986) 1253–1257.
[52] X. Bokhimi, A. Morales, A. García-Ruiz, T.D. Xiao, H. Chen, P.R. Strutt, J. Solid State Chem. 142 (2) (1999) 409–418.
[53] D. Wang, Y. Guo, K. Liang, K. Tao, Sci. China Ser. A 42 (1) (1999) 80–86.
[54] V.S. Stubican, R.C. Hink, S.P. Ray, J. Am. Ceram. Soc. 61 (1-2) (1978) 17–21.
[55] M. Kogler, E.M. Köck, B. Klötzer, S. Penner, J. Phys. Chem. C 120 (39) (2016) 22443–22454.
[56] M. Thommes, K. Kaneko, A.V. Neimark, J.P. Olivier, F. Rodriguez-Reinoso, J. Rouquerol, K.S.W. Sing, Pure Appl. Chem. 87 (9-10) (2015) 1051–1069.

[57] W. Brockner, C. Ehrhardt, M. Gjikaj, Thermochim. Acta 456 (1) (2007) 64–68.
[58] J.C. Duchet, M.J. Tilliette, D. Cornet, Catal. Today 10 (4) (1991) 507–520.
[59] H. Tagawa, J. Mizusaki, H. Narita, H. Takeuchi, Thermochim. Acta 163 (1990) 303–312.
[60] J. Li Vage, K. Doi, C. Mazieres, J. Am. Chem. Soc. 51 (6) (1968) 349–353.
[61] M.K. Dongare, K. Malshe, C.S. Gopinath, I.K. Murwani, E. Kemnitz, J. Catal. 222 (1) (2004) 80–86.
[62] G. Štefanić, M. Didović, S. Musić, J. Mol. Struct. 834-836 (2006) 435–444.
[63] S.K. Mohanty, G. Purohit, R.D. Purohit, P.K. Sinha, A. Mondal, B.B. Nayak, Int. J. Nanosci. 10 (4-5) (2011) 727–731.
[64] E.D. Silveira, R.C. Rabelo-Neto, F.B. Noronha, Catal. Today 289 (2017) 289–301.
[65] J.K. Kesavan, I. Luisetto, S. Tuti, C. Meneghini, G. Iucci, C. Battocchio, S. Mobilio, S. Casciardi, R. Sisto, J. CO2 Util. 23 (2018) 200–211.
[66] M.H. Youn, J.G. Seo, J.C. Jung, S. Park, D.R. Park, S.-B. Lee, I.K. Song, Catal. Today 146 (1-2) (2009) 57–62.
[67] M.H. Youn, J.G. Seo, S. Park, J.C. Jung, D.R. Park, I.K. Song, Int. J. Hydrogen Energy 33 (24) (2008) 7457–7463.
[68] W.-T. Zheng, K.-Q. Sun, H.-M. Liu, Y. Liang, B.-Q. Xu, Int. J. Hydrogen Energy 37 (16) (2012) 11735–11747.
[69] B.-Q. Xu, J.-M. Wei, Y.-T. Yu, J.-L. Li, Q.-M. Zhu, Top. Catal. 22 (1-2) (2003) 77–85.
[70] C.H. Bartholomew, R.B. Pannell, J.L. Butler, D.G. Mustard, Ind. Eng. Chem. Prod. RD 20 (2) (1981) 296–300.
[71] J.M. Montejano-Carrizales, J.L. Morán-López, Nanostruct. Mater. 1 (5) (1992) 397–409.
[72] Y. Zhao, W. Li, M. Zhang, K. Tao, Catal. Commun. 3 (2002) 239–245.
[73] Z.-Y. Ma, C. Yang, W. Wei, W.-H. Li, Y.-H. Sun, J. Mol. Catal. A-Chem. 227 (2005) 119–124.
[74] V. Bolis, C. Morterra, M. Volante, L. Orio, B. Fubin, Langmuir 6 (1990) 695–701.
[75] N.B. Jackson, J.G. Ekerdt, J. Catal. 126 (1990) 31–45.
[76] K. Pokrovski, K.T. Jung, A.T. Bell, Langmuir 17 (2001) 4297–4303.
[77] H. Chen, Y. Ding, N.T. Cong, B. Dou, V. Dupont, M. Ghadiri, P.T. Williams, Renew. Energy 36 (2) (2011) 779–788.
[78] X. Wang, S. Li, H. Wang, B. Liu, X. Ma, Energ. Fuel 22 (6) (2008) 4285–4291.
[79] B. Lee, J. Heo, S. Kim, C.-H. Kim, S.-K. Ryi, H. Lim, Energy Convers. Manage. 180 (2019) 250–257.
[80] R. Sundari, P.D. Vaidya, Energ. Fuel 26 (7) (2012) 4195–4204.
[81] R.S. Rao, A.B. Walters, M.A. Vannice, J. Phys. Chem. B 109 (2005) 2086–2092.
[82] J.M. González-Carballo, F.J. Pérez-Alonso, M. Ojeda, F.J. García-García, J.L. G. Fierro, S. Rojas, ChemCatChem 6 (2014) 2084–2094.
[83] S. Benard, L. Retailleau, F. Gaillard, P. Vernoux, A. Giroir-Fendler, Appl. Catal. B. Environ. 55 (2005) 11–21.
[84] P.J. Schmitz, R.J. Kudla, A.R. Drews, A.E. Chen, C.K. Lowe-Ma, R.W. McCabe, W. F. Schneider, C.T. Goralski, Appl. Catal. B: Environ. 67 (2006) 246–256.
[85] L.I. Godina, A.V. Kirilin, A.V. Tokarev, I.L. Simakova, D.Yu. Murzin, Ind. Eng. Chem. Res. 57 (6) (2018) 2050–2067.
[86] Z. Hou, J. Gao, J. Guo, D. Liang, H. Lou, X. Zheng, J. Catal. 250 (2) (2007) 331–341.
[87] C. Montero, A. Remiro, B. Valle, L. Oar-Arteta, J. Bilbao, A.G. Gayubo, Ind. Eng. Chem. Res. 58 (32) (2019) 14736–14751.
[88] C.K. Cheng, S.Y. Foo, A.A. Adesina, Catal. Today 178 (1) (2011) 25–33.
[89] A. Aho, S. Engblom, K. Eränen, V. Russo, P. Mäki-Arvela, N. Kumar, J. Wärnå, T. Salmi, D.Yu. Murzin, Chem. Eng. J. 405 (2021), 126945.
[90] S.E. Wanke, P.C. Flynn, Catal. Rev. 12 (1) (1975) 93–135.
[91] M.D. Argyle, C.H. Bartholomew, Catalysts 5 (1) (2015) 145–269.
[92] C.H. Bartholomew, Catal. Rev. 24 (1) (1982) 67–112.
[93] N.D. Charisiou, S.L. Douvartzides, G.I. Siakavelas, L. Tzounis, V. Sebastian, V. Stolojan, S.J. Hinder, M.A. Baker, K. Polychronopoulou, M.A. Goula, Catalysts 9 (8) (2019) 676–697.
[94] N.D. Charisiou, K.N. Papageridis, L. Tzounis, V. Sebastian, S.J. Hinder, M.A. Baker, M. AlKetbi, K. Polychronopoulou, M.A. Goula, Int. J. Hydrogen Energy 44 (1) (2018) 256–273.
[95] M. Velasquez, C. Batiot-Dupeyrat, J. Gallego, J.J. Fernández, A. Santamaria, Diam. Relat. Mater. 70 (2016) 105–113.
[96] C.K.S. Choong, Z. Zhong, L. Huang, Z. Wang, T.P. Ang, A. Borgna, J. Lin, L. Hong, L. Chen, Appl. Catal. A 407 (1–2) (2011) 145–154.
[97] M.A.A. Aziz, A.A. Jalil, S. Triwahyono, A. Ahmad, Green Chem. 17 (5) (2015) 2647–2663.
[98] B. Miao, S.S. Khine Ma, X. Wang, H. Su, S.H. Chan, Catal. Sci. Technol. 6 (12) (2016) 4048–4058.
[99] D. Chen, K.O. Christensen, E. Ochoa-Fernández, Z. Yu, B. Tøtdal, N. Latorre, A. Monzón, A. Holmen, J. Catal. 229 (1) (2005) 82–96.